

# JGR Atmospheres



## RESEARCH ARTICLE

10.1029/2021JD035728

### Key Points:

- We report the first observations of vertical fluxes of sensible heat & Na induced by the complete temporal spectrum of gravity waves
- McMurdo sensible heat and Na fluxes exhibit large downward peaks near 84 km and large upward sensible heat fluxes occur at ~97–106 km
- Sensible heat & Na flux measurements support theories and show significant impacts of wave-induced vertical transport and secondary waves

### Supporting Information:

Supporting Information may be found in the online version of this article.

### Correspondence to:

X. Chu and C. S. Gardner,  
[Xinzhao.Chu@colorado.edu](mailto:Xinzhao.Chu@colorado.edu);  
[cgardner@illinois.edu](mailto:cgardner@illinois.edu)

### Citation:

Chu, X., Gardner, C. S., Li, X., & Lin, C. Y.-T. (2022). Vertical transport of sensible heat and meteoric Na by the complete temporal spectrum of gravity waves in the MLT above McMurdo (77.84°S, 166.67°E), Antarctica. *Journal of Geophysical Research: Atmospheres*, 127, e2021JD035728. <https://doi.org/10.1029/2021JD035728>

Received 20 AUG 2021

Accepted 30 JUN 2022

### Author Contributions:

**Conceptualization:** Xinzhao Chu, Chester S. Gardner

**Data curation:** Xinzhao Chu, Xianxin Li, Cissi Ying-Tsen Lin

**Formal analysis:** Xinzhao Chu, Chester S. Gardner

**Funding acquisition:** Xinzhao Chu, Chester S. Gardner

© 2022. The Authors.

This is an open access article under the terms of the [Creative Commons Attribution-NonCommercial-NoDerivs](https://creativecommons.org/licenses/by-nc-nd/4.0/) License, which permits use and distribution in any medium, provided the original work is properly cited, the use is non-commercial and no modifications or adaptations are made.

## Vertical Transport of Sensible Heat and Meteoric Na by the Complete Temporal Spectrum of Gravity Waves in the MLT Above McMurdo (77.84°S, 166.67°E), Antarctica

Xinzhao Chu<sup>1</sup> , Chester S. Gardner<sup>2</sup> , Xianxin Li<sup>1,3</sup>, and Cissi Ying-Tsen Lin<sup>1,4</sup>

<sup>1</sup>Cooperative Institute of Research in Environmental Sciences & Department of Aerospace Engineering Sciences, University of Colorado Boulder, Boulder, CO, USA, <sup>2</sup>Department of Electrical and Computer Engineering, University of Illinois, Urbana, IL, USA, <sup>3</sup>Institute of Oceanographic Instrumentation, Qilu University of Technology, Shandong Academy of Sciences, Qingdao, China, <sup>4</sup>Department of Space Science & Engineering, National Central University, Taoyuan, Taiwan

**Abstract** We report the first lidar observations of vertical fluxes of sensible heat and meteoric Na from 78 to 110 km in late May 2020 at McMurdo, Antarctica. The measurements include contributions from the complete temporal spectrum of gravity waves and demonstrate that wave-induced vertical transport associated with atmospheric mixing by non-breaking gravity waves, Stokes drift imparted by the wave spectrum, and perturbed chemistry of reactive species, can make significant contributions to constituent and heat transport in the mesosphere and lower thermosphere (MLT). The measured sensible heat and Na fluxes exhibit downward peaks at 84 km ( $-3.0 \text{ Kms}^{-1}$  and  $-5.5 \times 10^4 \text{ cm}^{-2}\text{s}^{-1}$ ) that are ~4 km lower than the flux peak altitudes observed at midlatitudes. This is likely caused by the strong downwelling over McMurdo in late May. The Na flux magnitude is double the maximum at midlatitudes, which we believe is related to strong persistent gravity waves in the MLT at McMurdo. To achieve good agreement between the measured Na flux and theory, it was necessary to infer that a large fraction of gravity wave energy was propagating downward, especially between 80 and 95 km where the Na flux and wave dissipation were largest. These downward propagating waves are likely secondary waves generated in-situ by the dissipation of primary waves that originate from lower altitudes. The sensible heat flux transitions from downward below 90 km to upward from 97 to 106 km. The observations are explained with the fully compressible solutions for polarization relations of primary and secondary gravity waves with  $\lambda_z > 10 \text{ km}$ .

**Plain Language Summary** The upper atmosphere is filled with waves that originate in the lower atmosphere from storm systems and airflow over mountainous terrain, and then propagate upward. These waves play key roles in establishing the composition and temperature structures by mixing the upper atmosphere and by perturbing chemical reactions of important reactive species like atomic oxygen and ozone. By using meteoric sodium (Na) that is injected between 78 and 110 km altitude by the vaporization of cosmic dust, as a tracer, and exciting the Na atoms to fluorescence using a lidar system located at McMurdo Station, Antarctica, we directly measured the vertical transport of heat and Na induced by the full spectrum of waves. A surprising discovery is the positive heat flux in the lower thermosphere (97–106 km), which contradicts conventional thinking but demonstrates the importance of the fully compressible solutions for polarization relations of primary and secondary gravity waves. By comparing the measured Na transport with theory, we also show that many of the waves between 80 and 95 km are propagating downward, which are likely generated in this region when upward propagating waves become unstable and break, much like ocean waves behave when breaking over a shoal.

## 1. Introduction

The spectrum of atmospheric gravity waves drives the global circulation and controls the vertical transport of heat and constituents in the mesosphere and lower thermosphere (MLT). Dissipating waves exert a drag on the mean horizontal flow (Holton, 1982, 1983; Lindzen, 1981), while both dissipating and non-dissipating waves, induce strong vertical mixing of the atmosphere (Gardner et al., 2019; Hickey et al., 2000; Liu, 2021), alter molecular and eddy diffusion by perturbing constituent mixing ratios (Gardner, 2018; Grygalashvily et al., 2012), and drive the chemical transport of reactive species by modulating their chemical reactions (Gardner & Liu, 2010, 2016; Walterscheid & Schubert, 1989). Non-breaking gravity waves also induce a net heat flux (Walterscheid, 1981;

**Investigation:** Xinzhao Chu, Chester S. Gardner

**Methodology:** Xinzhao Chu, Chester S. Gardner

**Project Administration:** Xinzhao Chu

**Software:** Xinzhao Chu

**Supervision:** Xinzhao Chu

**Validation:** Xinzhao Chu

**Visualization:** Xinzhao Chu

**Writing – original draft:** Xinzhao Chu, Chester S. Gardner

**Writing – review & editing:** Xinzhao Chu, Chester S. Gardner

Weinstock, 1983) in addition to the diffusive heat transport caused by turbulence arising from breaking waves (Lindzen, 1981).

Wave-driven heat and constituent transport are characterized by the vertical fluxes of sensible heat and constituents, which are defined as the expected values of the product of the vertical wind fluctuations ( $w'$ ) and the temperature ( $T'$ ) or constituent density ( $\rho'_c$ ) fluctuations induced by the gravity wave spectrum. Observations of these important parameters are rare because it is necessary to measure simultaneously, over long periods of time, the vertical wind ( $w$ ), temperature ( $T$ ), and constituent number densities ( $\rho_c$ ), to derive statistically significant estimates of the fluxes. The first observations of sensible heat flux ( $\overline{w'T'}$ , overbar denotes sample average) in the MLT were reported from Haleakala, HI (20.7°N) using a Na Doppler lidar (Tao & Gardner, 1995) followed by more extensive observations at the Starfire Optical Range, NM (SOR, 35°N) (Gardner & Yang, 1998). Na flux ( $\overline{w'\rho'_{Na}}$ ) observations were first reported from SOR (Liu & Gardner, 2004) and then from Haleakala (Liu & Gardner, 2005). These observations have revealed that the heat and Na fluxes peak just below 90 km, with maximum downward (negative) values of  $-1$  to  $-3$  Km/s and  $-1 \times 10^4$  to  $-3 \times 10^4$  cm<sup>2</sup>s<sup>-1</sup> (Gardner & Liu, 2007, 2010). More significantly, the heat flux convergence induces strong cooling near 90 km that can approach  $-50$  Kd<sup>-1</sup> for the annual mean (Gardner & Liu, 2007). Furthermore, the large downward Na flux near 90 km is 5–10 times larger than the expected eddy flux, which implies that the cosmic dust influx, the source of all the mesospheric metal layers, is much larger than previously assumed (Carrillo-Sánchez et al., 2016). More recently, the Fe and Na fluxes were measured simultaneously at Table Mountain, CO (40°N). These observations have demonstrated that the cosmic dust particles responsible for injecting a large fraction of the ablated material into the Earth's upper atmosphere enter at relatively slow speeds and originate primarily from the Jupiter Family of Comets (Carrillo-Sánchez et al., 2015, 2016; Huang et al., 2015). Long-term Na lidar observations of gravity wave momentum, heat and Na fluxes conducted at Hefei, China (32°N), exhibit smaller values for all three parameters (Tao Li, private communication, University of Science and Technology of China), which may reflect significant differences in wave activity at this site compared to SOR, Haleakala, and Table Mountain. Most recently, sensible heat and potential temperature fluxes ( $\overline{w'\theta'}$ ,  $\theta$  = potential temperature) have been reported from Cerro Pachón in the Chilean Andes (30°S), which are more in line with the profiles observed at SOR and Haleakala (Guo & Liu, 2021).

All these previous measurements of heat and constituent fluxes were made at mid-latitudes by employing nighttime data with observation periods less than about 8–10 hr, which do not include the effects of inertial-period gravity waves. Here, we report the first lidar measurements of the vertical fluxes of meteoric Na and sensible heat at extremely high latitudes using vertical wind, temperature, and Na observations, made at McMurdo Station (77.84°S, 166.67°E) in May 2020. Because the inertial period at McMurdo is 12.3 hr, and the two observation periods utilized for this study each exceeded 16 hr, the derived fluxes represent contributions of the complete gravity wave temporal spectrum from the inertial frequency ( $f$ ) to the buoyancy frequency ( $N$ ).

In contrast to the previous reports of fluxes between 85 and 100 km at midlatitudes, the acquisition of high-quality lidar data at McMurdo (Chu et al., 2020) and application of an innovative data processing technique (Gardner & Chu, 2020) have enabled the extension of flux measurements into the lower thermosphere (100–110 km) and below 85 km to nearly 75 km. A surprising discovery is the positive (upward) sensible heat flux between 97 and 106 km, which contradicts the traditional understanding of wave-driven heat transport, but aligns well with the earlier findings of super-exponential growth of tidal and planetary wave amplitudes in temperature from 100 to 110 km (Fong et al., 2014, 2015; Lu, Chu, Chen, et al., 2017). We show that the positive heat fluxes are predicted by the fully compressible solutions for the polarization relations (Vadas, 2013) of upward-propagating, non-dissipative gravity waves. When the spectrum is dominated by energetic waves with mesoscale vertical wavelengths ( $\lambda_z \sim 20$  km), as is predicted by models (Vadas & Becker, 2019; Vadas et al., 2018) and is often observed in the lower thermosphere (e.g., Chen et al., 2016; Chu, Yu, et al., 2011), the phase difference between  $w'$  and  $T'$  is about 8°–9° less than 90°, and consequently, the positive heat flux is expected to approach several +Kms<sup>-1</sup>. The presence of external heat sources and/or wave amplification in the lower thermosphere over McMurdo may also contribute to the positive heat flux, possibly via introducing additional phase shift between  $w'$  and  $T'$  by energy input and forcing from the magnetosphere and ion-neutral coupling or via wave amplification caused by large wind shears and instabilities. The McMurdo flux profiles are compared to those previously observed at several mid-latitude sites and show that wave-driven atmospheric mixing plays a significant role in establishing the thermal and constituent structures of the polar upper atmosphere. In particular, the comparison of the measured Na

flux profile with theory demonstrates the importance of vertical Stokes drift induced by the full wave spectrum, chemical transport for chemically active species like Na, and the influence of downward-propagating waves, especially in regions of strong wave dissipation. The Na and heat fluxes at McMurdo peak near 84 km with values of about  $-5.5 \times 10^4 \text{ cm}^{-2}\text{s}^{-1}$  and  $-3.0 \text{ Km/s}$ , respectively, compared to  $\sim 88 \text{ km}$  at mid-latitudes with values about one half to one third as large for the Na flux. We hypothesize that these differences are caused by strong downwelling over the polar cap at this time of year and strong atmospheric mixing by both dissipating and non-dissipating gravity waves, including the long-period persistent gravity waves discovered at McMurdo (Chen et al., 2013, 2016).

## 2. McMurdo Lidar Data Acquisition and Processing

The McMurdo lidar campaign was conducted by the University of Colorado Boulder through a collaboration between the United States Antarctic Program (USAP) and Antarctica New Zealand (AntNZ) (Chu, Huang, et al., 2011; Chu, Yu, et al., 2011). The STAR (Student Training and Atmospheric Research) Na Doppler lidar was installed into the AntNZ laboratory at Arrival Heights Observatory (77.84°S, 166.67°E) in Jan 2018 (Chu et al., 2020), where it has since been operated alongside an Fe Boltzmann temperature lidar (not used in this study) that was installed in 2011. McMurdo is located at the edge of polar cap and auroral oval (Fong et al., 2014, 2015), and it is also a hotspot for gravity waves (Chen & Chu, 2017; Chen et al., 2013, 2016; Chu et al., 2018; Zhao et al., 2017) and planetary waves (Lu et al., 2013; Lu, Chu, Chen, et al., 2017). Long dark nights in winter months enable the Na lidar to make high-resolution measurements of Na, temperature, and vertical winds covering the complete temporal spectrum of gravity waves from the buoyancy period ( $\sim 5 \text{ min}$ ) to the inertial period ( $\sim 12.3 \text{ hr}$ ).

The STAR Na lidar employs the 3-frequency ratio technique to infer simultaneously the temperature ( $T$ ), vertical wind ( $w$ ), and atomic Na number density ( $\rho_{\text{Na}}$ ) in the MLT region (e.g., Chu & Papen, 2005). The laser transmitter operates at the Na  $D_{2a}$  wavelength of 589.15826 nm and at a pulse repetition rate of 50 pps with a single pulse energy of  $\sim 10\text{--}20 \text{ mJ}$ . The local oscillator laser is frequency-locked to the  $D_{2a}$  peak frequency by employing saturation-absorption spectroscopy, and then the output beam is frequency-shifted by  $\pm 750 \text{ MHz}$  using dual acousto-optic modulators to achieve 3-frequency operation (e.g., She & Yu, 1994). With an 81-cm diameter Newtonian telescope, the STAR lidar power-aperture product (PA) is between 0.25 and  $0.5 \text{ Wm}^2$ . The photo detector is a Hamamatsu H7421-40 photomultiplier tube (PMT, modified version) with a quantum efficiency (QE) of 40%. The high-efficiency receiver architecture (Smith & Chu, 2015), coupled with the high-QE PMT, produces large signal counts enabling high-resolution measurements even at the edges of the Na layer. For the data employed in this study, the Na densities, and hence the signal levels, varied over a dynamic range of more than 3 orders of magnitude. The PMT response curve was carefully measured and calibrated over this wide dynamic range to eliminate signal distortion caused by PMT nonlinearities, which, if not corrected, can affect heat flux measurements, especially at very high signal levels sometimes encountered near the peak of the Na layer (Liu & Guo, 2016). Detailed system specifications can be found in the Supporting Information of Chu et al. (2020).

The lidar data acquisition (DAQ) system saves the 3-frequency raw photon counts at fundamental resolutions of 4.5 s (1.5 s per frequency) in time ( $t$ ) and 24 m in altitude ( $z$ ). In post processing, the odd and even photon count samples in time are integrated separately to achieve the desired temporal and vertical resolutions, which for this study are  $\Delta t = 2.5 \text{ min}$  and  $\Delta z = 0.96 \text{ km}$ . This yields two statistically independent photon count profiles for each of the 3 laser frequencies that are interleaved in time and offset by the 4.5 s fundamental temporal resolution. Note, by independent, we mean that the photon noise contaminating each of the profiles is uncorrelated with the noise contaminating any other profile. However, because of the small 4.5 s offset, the gravity wave fluctuations that perturb the two interleaved photon count profiles are virtually perfectly correlated. This is equivalent to probing the same region of the atmosphere with two different lidars. The interleaved profiles are added when deriving the basic atmospheric parameters of  $T$ ,  $w$ , and  $\rho_{\text{Na}}$  along with their uncertainties ( $\Delta T$ ,  $\Delta w$ , and  $\Delta \rho_{\text{Na}}$ ). However, to eliminate photon noise biases when computing variances and fluxes, two statistically independent profiles of  $T$ ,  $w$ , and  $\rho_{\text{Na}}$  are derived from the interleaved photon counts, which are then used to compute independent profiles of  $w'$ ,  $T'$ , and  $\rho'_{\text{Na}}$ , where the prime denotes the fluctuation quantity. These independent fluctuation profiles are used to compute the variances and fluxes as described by Gardner and Chu (2020). This interleaved approach eliminates the photon noise biases and produces accurate estimates of variances and fluxes, provided the number of data samples is sufficiently large, which is the case for McMurdo Na Doppler lidar data set. Bias elimination is especially important in enabling the flux and fluctuation variance measurements to be extended into the



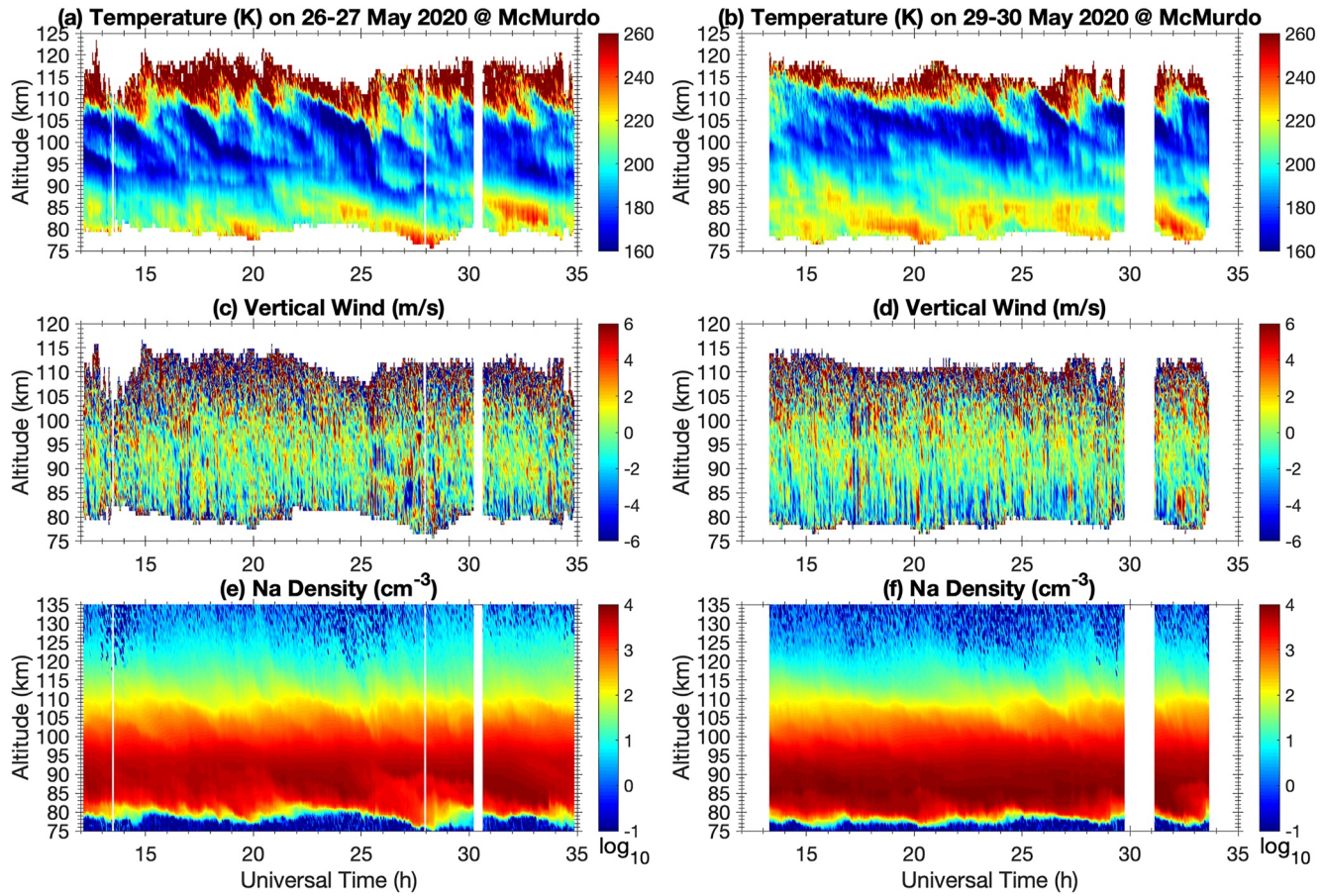


**Figure 1.** Contour plots of (top) temperature, (middle) vertical wind, and (bottom) Na density observed in the MLT at McMurdo, Antarctica during 26–27 and 29–30 May 2020 with the University of Colorado Na Doppler lidar. The data resolutions are  $\Delta t = 2.5$  min and  $\Delta z = 960$  m. The Na density is plotted in log-10 scale. The upward wind is positive.

thermosphere above 100 km and below 85 km where measurement uncertainties increase substantially because of the low signal levels caused by decreasing Na densities.

### 3. Fundamental Atmospheric Observations

Observations of MLT temperatures, vertical winds, and Na densities on 26–27 May 2020 and 29–30 May 2020 at McMurdo are illustrated in Figure 1. The mean temperature ( $\bar{T}$ ), lapse rate ( $-\partial\bar{T}/\partial z$ ), and Na density ( $\bar{\rho}_{\text{Na}}$ ) profiles and their errors are plotted in Figure 2. A striking feature is the rich spectrum of gravity waves. Temperature perturbations are dominated by persistent, low-frequency gravity waves with periods of 3–10 hr (Chen & Chu, 2017; Chen et al., 2016), while vertical wind perturbations are dominated by high-frequency gravity waves with periods less than  $\sim 1$  hr. These high-frequency waves are clearly visible in the temperature contours but with much smaller amplitudes than the persistent waves. Similarly, the low-frequency waves are visible in the vertical wind contours but with smaller amplitudes. This is consistent with the gravity wave polarization relations  $|w'| \simeq \frac{\omega g}{N^2} \frac{|T'|}{\bar{T}}$ , where  $\omega$  is the intrinsic frequency,  $g = 9.5$  m/s<sup>2</sup> is the gravitational acceleration, and  $N \simeq 2\pi/5$  min is the buoyancy frequency, so that the vertical wind perturbations increase with increasing intrinsic frequency. Note, the measurements illustrated in Figure 1 include the Doppler effects associated with the background wind field. Hence, the parameter fluctuation spectra represent the observed, not the intrinsic, frequencies, which under certain circumstances can be substantially different and where downward phase progression does not necessarily indicate upward energy propagation.

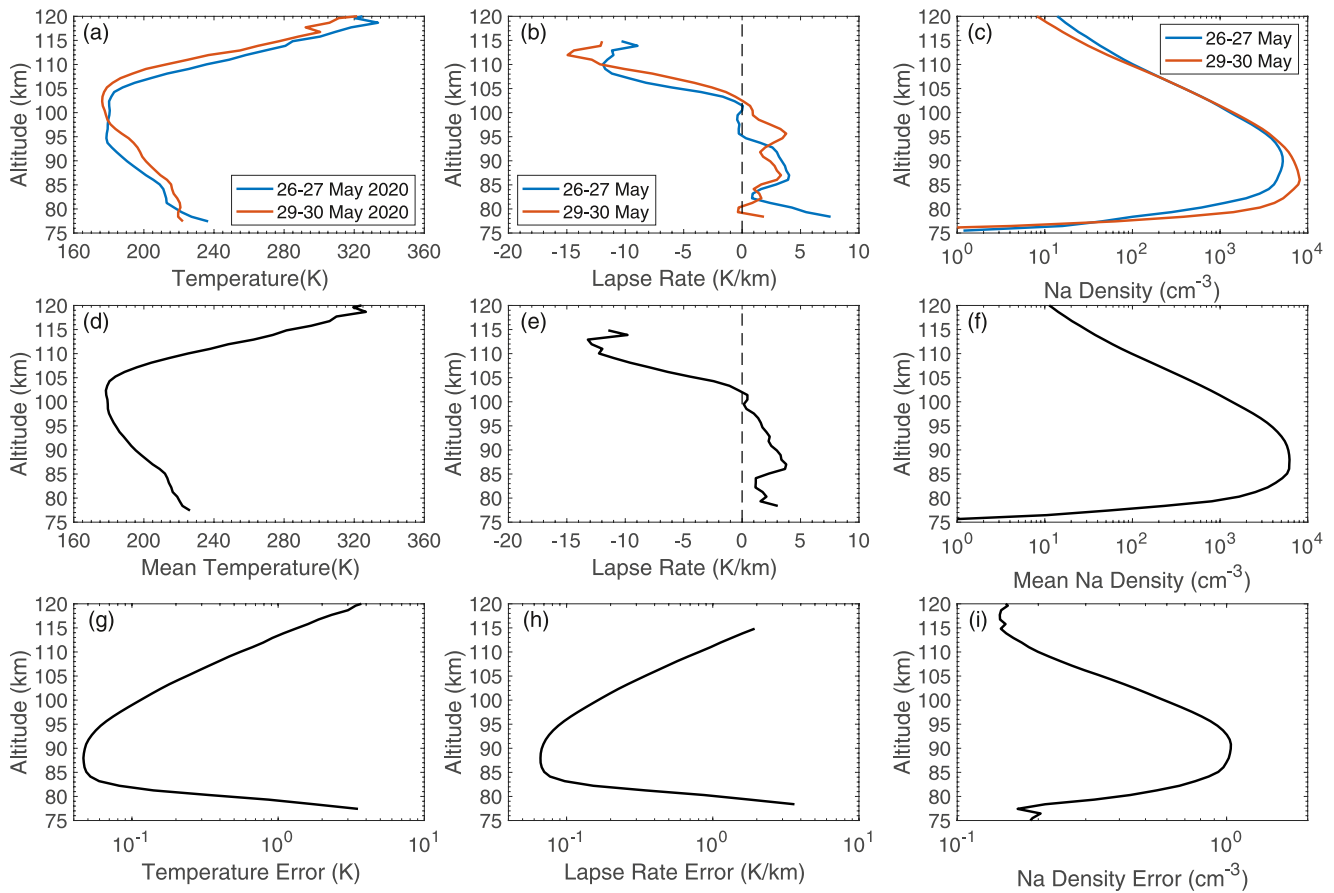


**Figure 2.** Profiles of (a) mean temperature, (b) lapse rate, and (c) Na density observed in the MLT at McMurdo, Antarctica during 26–27 and 29–30 May 2020 with the University of Colorado Na Doppler lidar. Profiles of the overall mean temperature ( $\bar{T}$ ), lapse rate ( $-\partial\bar{T}/\partial z$ ), and Na density ( $\bar{\rho}_{Na}$ ) profiles and their RMS uncertainties are plotted in panels (d)–(i). The lapse rate profiles in panels (b and e) were smoothed with a Hamming window with a full width of 2.5 km.

Another interesting feature observed in Figure 2c is the low peak altitudes of Na layers. Both lidar runs show the Na layer peak below 90 km, and the peak on 29–30 May 2020 is close to 85 km. The Na layers measured at midlatitudes have peaks usually above 90 km, even during winter (e.g., Gardner & Liu, 2010; Guo & Liu, 2021). Furthermore, the Na layers at McMurdo extend below 80 km, giving sufficient signal for deriving temperature and vertical wind below 80 km. This situation is very different from the midlatitude observations where Na signals typically fall quickly below 85 km. The layer bottom-side extension at McMurdo is clearly illustrated in Figures 2c and 2f. Even at 78 km, the mean Na density is still above 100 cm<sup>-3</sup>, enabling the measurements of temperature and its lapse rate. The Na layer peak altitude on 26–27 May 2020 is higher than on 29–30 May 2020, but both runs exhibit small temperature inversion layers with the peak inversion around 84–85 km (Figure 2a), which, as discussed later, may be associated with wave dissipation and heat transport. For the overall mean temperature profile in Figure 2d, the mesopause is located at 102.4 km and there is a small inversion peak at 85 km, which causes a sharp increase in the environmental lapse rate above 85 km. The lapse rate ( $-\partial\bar{T}/\partial z$ ) of the overall mean temperature is positive below the mesopause but becomes negative and grows quickly above the mesopause. The small temperature inversion layer leads to the largest lapse rate of about 4 K/km at 86.5 km. It is worth noting that simultaneous measurements by the Fe Boltzmann lidar show the same mesopause features and temperature inversion layers around 85 km, while the observed Fe layers (not shown) also exhibit low peak altitudes and downward extension of the layer bottom sides like the Na layers.

Figures 3a–3d illustrate the variances of temperature, environmental lapse rate, vertical wind, and Na number density perturbations in the MLT that were induced by the complete temporal spectrum of gravity waves. As discussed in Section 2, to eliminate photon noise biases, which can be especially large at the extreme altitudes where the signal levels are small, these variance profiles were derived using the interleaved data sets according

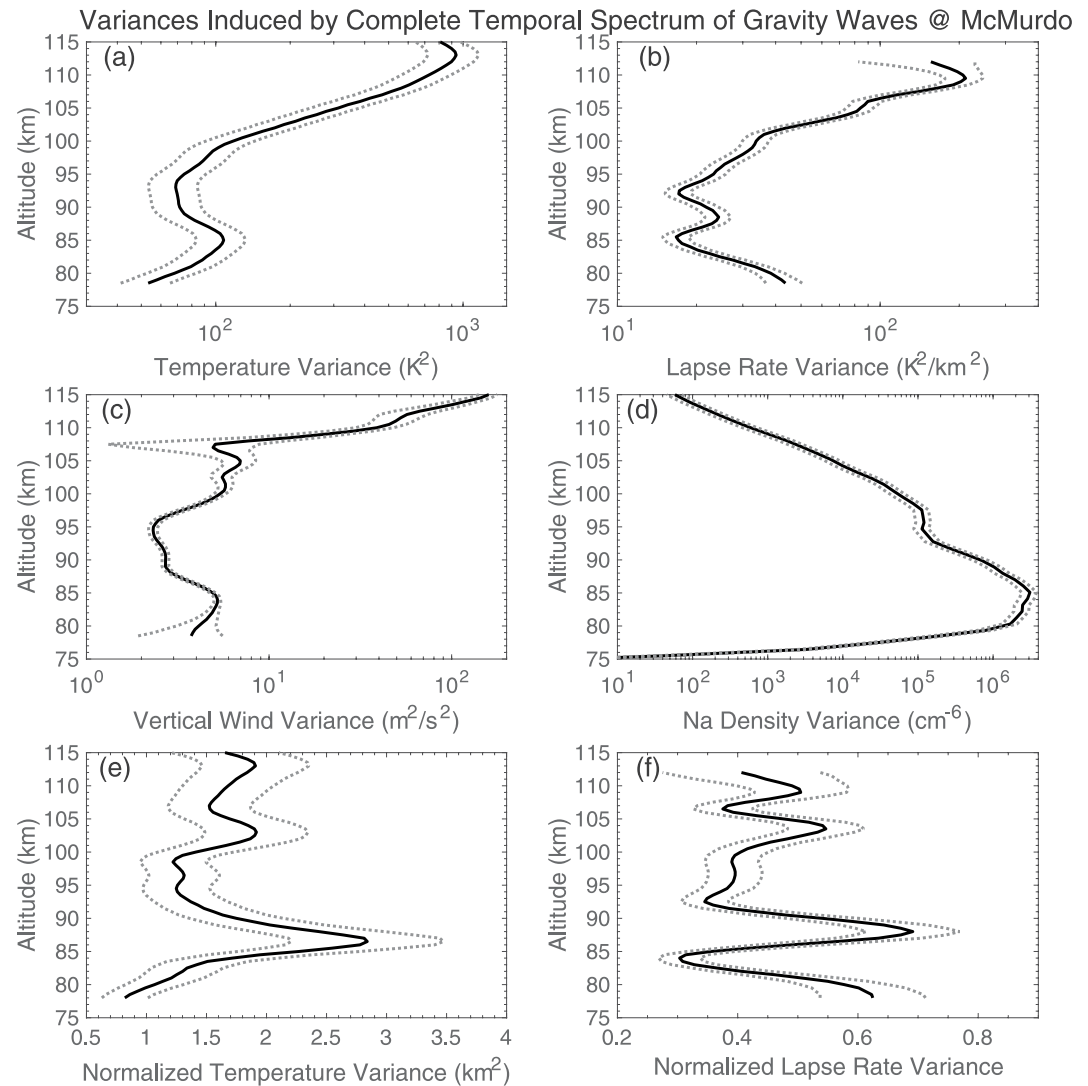


**Figure 3.** Profiles of the computed fluctuation variances of (a) temperature  $\text{Var}(T') = \overline{(T')^2}$ , (b) lapse rate  $\text{Var}(-\partial T'/\partial z) = \overline{(\partial T'/\partial z)^2}$ , (c) vertical wind  $\text{Var}(w') = \overline{(w')^2}$ , and (d) Na density  $\text{Var}(\rho'_{\text{Na}}) = \overline{(\rho'_{\text{Na}})^2}$  induced by the complete temporal spectrum of gravity waves in the MLT at McMurdo, Antarctica during 26–27 and 29–30 May 2020. Profiles of the (e) normalized temperature variance  $\text{Var}(T') / (\Gamma_{\text{ad}} + \partial \bar{T} / \partial z)^2$  and (f) normalized lapse rate variance  $\text{Var}(-\partial T' / \partial z) / (\Gamma_{\text{ad}} + \partial \bar{T} / \partial z)^2$ . The profiles were smoothed with a 5 km full width Hamming window. The rms uncertainties (error bars) are plotted as gray-dotted curves.

to the processing procedure described by Gardner and Chu (2020). The temperature, vertical wind, and Na density fluctuations were computed by subtracting the temporal means for each of the two observation periods. The variance profiles have been smoothed using a Hamming window with a full width of 5 km to reduce the uncertainties, especially the contributions from photon noise (see Figure S1 in Supporting Information S1 for plots of the unsmoothed profiles). The smoothed variance profiles include the unattenuated contributions from waves with vertical wavelengths as small as  $2\Delta z = 1.92$  km, but the resolution of variance profiles has been reduced to about 3.42 km (rectangular window equivalent) by applying the Hamming window smoothing function. The root-mean-square (rms) uncertainties (error bars) were computed according to Appendix B and plotted as gray-dotted curves in Figure 3. We also computed and plotted the normalized temperature and lapse rate variances in Figures 3e and 3f, where the normalization factor is  $(\Gamma_{\text{ad}} + \partial \bar{T} / \partial z)^2$ ,  $\Gamma_{\text{ad}} = g/C_p$  is the dry adiabatic lapse rate, and  $C_p = 1003 \text{ m}^2\text{K}^{-1}\text{s}^{-2}$  is the specific heat at constant pressure. The normalized

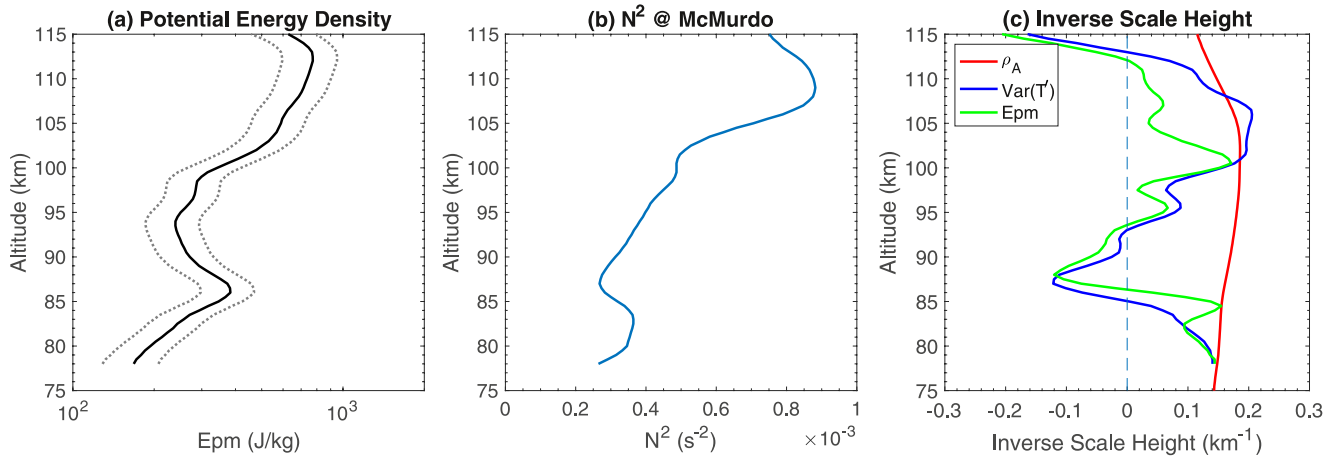


**Figure 4.** Profiles of the (a) potential energy per unit mass, (b) square of buoyancy frequency, and (c) inverse scale heights of atmospheric density, temperature variance, and potential energy per unit mass for the MLT above McMurdo in late May 2020. The  $E_{pm}$  and  $N^2$  profiles were smoothed with a 5 km full-width Hamming window and the inverse scale heights were computed from smoothed profiles. The RMS uncertainties (error bars) of  $E_{pm}$  are plotted as gray-dotted curves in (a).

temperature variance is approximately equal to the mean-square value of the displacements imparted to the atmosphere by the spectrum of waves. It is correlated with the strength of the vertical wind fluctuations and is therefore a measure of the degree of vertical mixing induced by the waves. The normalized lapse rate variance is approximately equal to the mean of the inverse Richardson number (Ri) and is a measure of the instability of the atmosphere through which the waves are propagating (see Appendix A, Equation A9). These normalized, fluctuation variance profiles suggest that between 86 and 92 km is a region of high instability and vigorous atmospheric mixing. Notice that the temperature contours in Figure 1 are disorganized in this region but exhibit distinct wave signatures with downward phase progression above and below. The normalized variances will be used later to calculate the gravity wave potential energy per unit mass ( $E_{pm}$ ) and to estimate the fraction of wave energy propagating downward ( $\alpha_{down}$ ).

The temperature variance  $\text{Var}(T')$  profile in Figure 3 exhibits a local maximum (peak) of  $\sim 110 \text{ K}^2$  at  $\sim 85 \text{ km}$  where the small peak of the temperature inversion is located in Figure 2. A minimum lapse rate variance  $\text{Var}(-\partial T'/\partial z)$  of  $\sim 14 \text{ K}^2/\text{km}^2$  and a maximum Na density variance  $\text{Var}(\rho'_{Na})$  of  $\sim 3.1 \times 10^6 \text{ cm}^{-6}$  occur at similar altitudes. The vertical-wind variance  $\text{Var}(w')$  has a local maximum of  $5.7 \text{ m}^2/\text{s}^2$  around 84 km. After a decrease above 85 km, the temperature variance starts to increase above 94 km and grows rapidly above 100 km, alongside the growth of the lapse rate variance. The potential energy per unit mass  $E_{pm}$  of the gravity wave spectrum is computed from the temperature variance and square of buoyancy frequency ( $N^2$ ) measured by the lidar

$$E_{pm} \simeq \frac{1}{2} \frac{g^2}{N^2(\bar{T})^2} \overline{(T')^2} = \frac{N^2}{2} \frac{\text{Var}(T')}{(\Gamma_{ad} + \partial \bar{T}/\partial z)^2}. \quad (1)$$

Although we use this expression for  $E_{pm}$ , its validity diminishes for the highest wave frequencies near the buoyancy frequency, which our data include. The  $E_{pm}$  and  $N^2$  profiles are shown in Figures 4a and 4b, respectively. The inverse scale heights for the atmospheric density (red curve),  $\text{Var}(T')$  (blue curve) and  $E_{pm}$  (green curve) are plotted for comparison in Figure 4c. The atmospheric density profile, used to calculate the scale height, was obtained from the atmosphere model NRLMSISE-00 (Picone et al., 2002). As expected for dissipating gravity waves, the inverse scale heights for  $\text{Var}(T')$  and  $E_{pm}$  are smaller than for  $\rho_A$  throughout most of the range between 80 and 115 km. In fact, dissipation is so strong between 86 and 92 km and above 112 km that the inverse scale heights are negative, reflecting the reduction of wave amplitudes with increasing altitude in these regions. The high instability and vigorous mixing (as indicated by the normalized variances of lapse rate and temperature in Figure 3) along with the local minima of  $\text{Var}(T')$  and  $E_{pm}$  and the negative scale heights suggest that the strongest wave dissipation and gravity wave breaking occur in this region of  $\sim 86$ – $92 \text{ km}$ . However, near 100 km, all three inverse scale heights are comparable indicating negligible wave dissipation, while between 101 and 108 km the temperature variance increases faster than  $1/\rho_A$  which may be an indication that some waves are being amplified



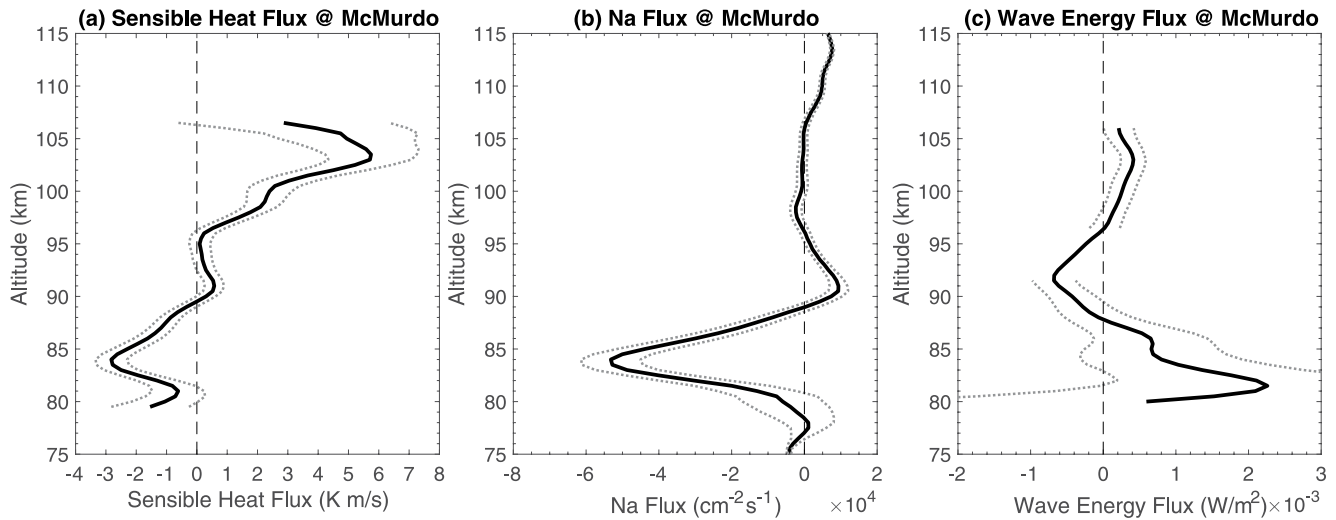


**Figure 5.** Profiles of the vertical fluxes of (a) sensible heat ( $\overline{w'T'}$ ), (b) Na ( $\overline{w'\rho'_{Na}}$ ), and (c) gravity wave energy ( $\overline{w'p'}$ ) observed in the MLT at McMurdo in late May 2020. The RMS uncertainties (error bars) of fluxes are plotted as gray-dotted curves. The energy flux profile was derived from the measured heat and Na flux profiles and by using the mean pressure profile from the atmospheric model NRLMSISE-00 (Picone et al., 2002).

(Fong et al., 2014, 2015; Lu, Chu, Chen, et al., 2017). Although the evidence suggests that dissipation is the primary source of  $E_{pm}$  decay between 86 and 92 km, as noted by a reviewer, other potential channels for the decrease (or increase) in  $E_{pm}$  are the conversions between wave potential and kinetic energies and between wave potential energy and the mean potential energy. Both conversions are driven by the potential temperature flux and can proceed either way.

The  $E_{pm}$  profile in Figure 4a exhibits a striking similarity in shape to the  $E_{pm}$  profile published in Figure 20 of Vadas and Becker (2019). These authors used numerical modeling to explore secondary and tertiary gravity wave generation over the Southern Andes. Their  $E_{pm}$  profile was derived by averaging the modeled, wave-driven potential energy density over the region from 279 to 296°E and 55.1–29.6°S for July 23 (mid-winter). In Vadas and Becker (2019),  $E_{pm}$  increases from the troposphere with increasing altitude, reaching a local maximum at ~85 km (like McMurdo), and then decreases in the height range between ~85 and ~94 km (also like McMurdo). The authors attribute the decrease to the breaking of primary waves that were launched in the lower atmosphere, which leads to the generation of secondary waves in the mesopause region. Above ~94 km, the amplitudes of the secondary waves increase with increasing altitude and reach another local maximum at ~112 km (like McMurdo). The decrease of  $E_{pm}$  between ~115 and 125 km occurs where most of the secondary gravity waves dissipate, leading to the generation of tertiary gravity waves (Vadas & Becker, 2019). Above McMurdo, the measured  $E_{pm}$  profile also exhibits local maxima at ~85 and ~112 km which is quite similar to the Vadas and Becker (2019) results, although the measured McMurdo  $E_{pm}$  at 112 km is about half the modeled value for the Southern Andes region. Such similarities suggest that secondary and tertiary gravity waves are also generated in the MLT above McMurdo via the multistep vertical coupling process that was proposed by Vadas and Becker (2018, 2019). Because the secondary and tertiary waves propagate both upward and downward, this mechanism could potentially lead to substantial fractions of downward-propagating gravity waves throughout the MLT region at McMurdo.

#### 4. Vertical Flux Observations

The vertical fluxes of sensible heat ( $\overline{w'T'}$ ) and Na density ( $\overline{w'\rho'_{Na}}$ ) were computed using the interleaved data at resolutions of  $\Delta z = 0.96$  km and  $\Delta t = 2.5$  min and then averaged over the two observation periods. This approach eliminates the small biases associated with partially correlated photon noise errors in the derived values of  $w'$ ,  $T'$  and  $\rho'_{Na}$  (Gardner & Chu, 2020). The results are plotted in Figure 5 after vertically smoothing using a Hamming window with a full width of 5 km (see Figure S2 in Supporting Information S1 for plots of the unsmoothed profiles). Because the resolution of the lidar data processing excluded the smaller-scale turbulence fluctuations, these profiles represent the vertical fluxes induced by gravity waves (not turbulence) with vertical wavelengths greater than  $2\Delta z = 1.92$  km and frequencies spanning the full temporal spectrum from  $f$  to  $N$ , in the region below



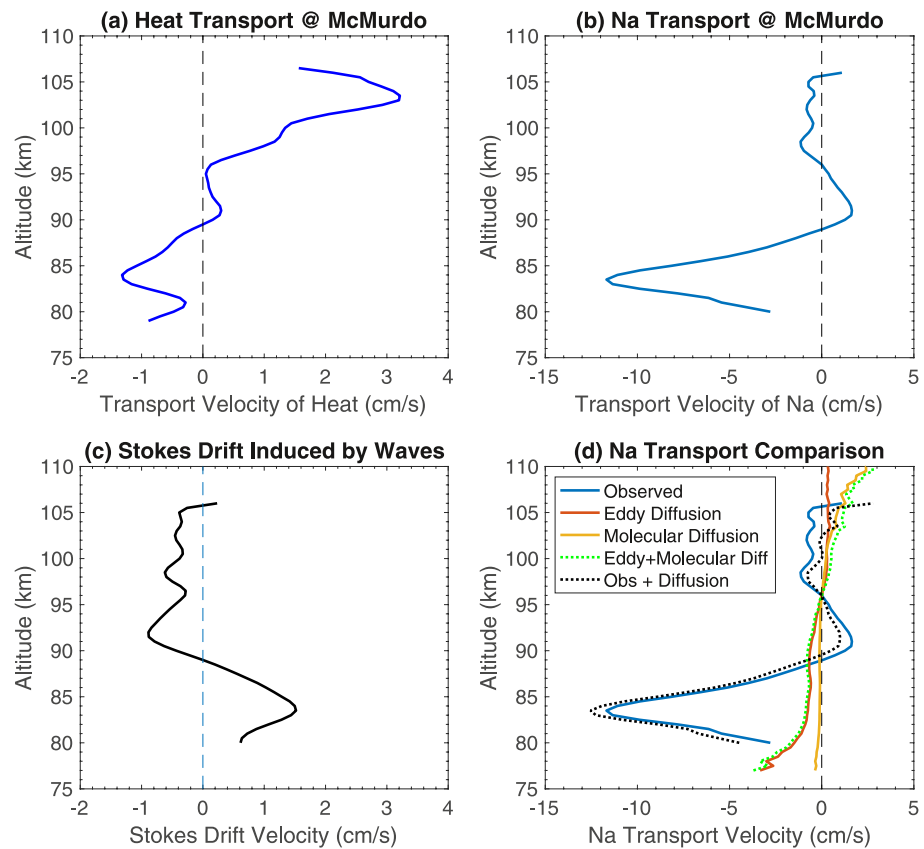


**Figure 6.** (a) Transport velocity of heat, and (b) Na, and (c) the Stokes drift velocity induced by the complete temporal spectrum of gravity waves at McMurdo in late May 2020. (d) Comparison of the observed Na transport velocity induced by non-breaking gravity waves with those induced by molecular and eddy diffusion.

100 km, where the buoyancy period is 5 min or longer. Above 100 km, where the buoyancy period is as short as 3.5 min (@110 km), the data exclude the highest frequency waves. However, the temperature, Na, and horizontal wind spectra are dominated by medium- and low-frequency waves, so the missing high-frequency wave energy is small. The data were not high-pass filtered so the fluxes may also include contributions from tides and planetary waves with periods up to ~40 hr, although because of their small vertical wind and temperature amplitudes, those contributions should be insignificant. The measurements exclude the smaller flux contributions from eddy and molecular diffusion which were not resolved. The Na flux is generally downward with the largest negative values between 80 and 90 km and a maximum value of about  $-5.5 \times 10^4 \text{ cm}^{-2} \text{ s}^{-1}$  at 84 km where the sensible heat flux also exhibits its maximum downward value of about  $-3.0 \text{ Kms}^{-1}$ . This altitude range of 80–90 km is a region of enhanced wave dissipation, which contains the local maxima in the temperature variance, normalized temperature variance, normalized lapse rate variance, and  $E_{\text{pm}}$  (Figures 3a, 3e, 3f, and 4a).

The wave-induced, vertical transport velocities of sensible heat  $\overline{w'T'}/\overline{T}$  and Na  $\overline{w'\rho'_{\text{Na}}}/\overline{\rho_{\text{Na}}}$  are plotted in Figures 6a and 6b. The heat transport velocity profile exhibits a downward peak of  $-1.3 \text{ cm/s}$  at 84 km and an upward peak of  $+3.2 \text{ cm/s}$  at 103 km. In comparison, the downward Na transport velocity reaches  $-11.7 \text{ cm/s}$  at ~84 km, which is more than double of the peak values observed at midlatitudes. The Na transport is slow and upward (positive) from 89 to 96 km and the small values are less than 2 cm/s. From 97 to 106 km, the Na transport is slightly downward with small values about  $-1 \text{ cm/s}$ . Note that the transport velocities shown in Figure 6 are the velocities relative to the background atmosphere, not relative to the ground. This is because the background vertical wind has been subtracted in the derivation of  $w'$  and the fluxes.

Heat and/or Na flux observations have been reported from six sites in both the northern and southern hemispheres and the key results are summarized in Table 1. Compared to other observations made at mid-latitudes in both hemispheres, the heat and Na fluxes at McMurdo reach their maximum downward values at a considerably lower

**Table 1**  
*Summary of Sensible Heat and Na Flux Observations in the Mesopause Region*

Site	Table Mountain, Colorado	SOR, New Mexico	Hefei, China	Maui, Hawaii	Cerro Pachón, Chile	McMurdo, Antarctica
References	Huang et al. (2015)	Gardner and Liu (2007, 2010)	Tao Li (Private Comm.)	Liu and Gardner (2005)	Guo and Liu (2021)	This Paper
Latitude	40.1°N	35.0°N	32°N	20.7°N	30.25°S	77.84°S
Longitude	105°W	106.5°W	117°E	156.3°W	70.74°W	166.7°E
Inertial period (h)	18.6	20.9	22.6	33.9	24.0	12.3
Observation length (h)	~5	~7.6	~10	~6.6	~5	~20
Observation period	Aug/Sep	Late Nov	Fall Mean	Annual Mean	June	Late May
Time resolution $\Delta t$ (min)	10	1.5	10	1.5	1	2.5
Alt. Resolution $\Delta z$ (km)	0.96	0.5	~3	0.96	2	0.96
Heat flux peak (K m/s)	N/A	−2.5	−0.3	−1.4	−2.8	−3.0
Heat flux peak altitude (km)	N/A	88	88	87–95	88–94	84
Na flux peak ( $10^4 \text{ cm}^{-2} \text{ s}^{-1}$ )	−1.5	−2.25	−0.3	−0.8	N/A	−5.5
Na flux peak altitude (km)	86	88	89–95	88	N/A	84

altitude and for the Na flux, the magnitude is larger. The seasonal variations of sensible heat flux at the Starfire Optical Range, NM (SOR, 35°N) exhibit strong semi-annual variations with maximum downward values of  $-2$  to  $-3$  K m/s at about 88 km altitude from early Nov to early Feb and minimum values of about  $-0.5$  K m/s at the equinoxes (Gardner & Liu, 2007). The Na flux at SOR also exhibits strong semi-annual variations with maximum values ranging from  $-1.75 \times 10^4 \text{ cm}^{-2} \text{ s}^{-1}$  to  $-2.75 \times 10^4 \text{ cm}^{-2} \text{ s}^{-1}$  at 88 km, from early Nov to early Feb and minimum values of about  $-0.25 \times 10^4 \text{ cm}^{-2} \text{ s}^{-1}$  at the equinoxes (Gardner & Liu, 2010). The late May McMurdo observations reported here correspond to late Nov measurements at SOR. The heat flux values for late fall are comparable at the two sites, but the peak altitude is about 4 km lower at McMurdo, which may simply reflect the stronger wintertime downwelling induced by the (residual) meridional circulation system at this high polar latitude. The peak value of the downward Na flux at McMurdo is more than twice the value observed at SOR, even though the Na density at 84 km at McMurdo in late May ( $\sim 5,000 \text{ cm}^{-3}$ ) is somewhat smaller than the Na density at 88 km at SOR in late Nov ( $\sim 6,500 \text{ cm}^{-3}$ ). As will be discussed in Section 6, the larger Na flux at McMurdo appears to be associated with more intense wave activity as reflected in variance of the temperature fluctuations ( $\sim 105 \text{ K}^2$  @ 84 km for McMurdo vs.  $\sim 60 \text{ K}^2$  @ 88 km for SOR). This is not surprising since the McMurdo Na flux measurements include the contributions from the complete temporal spectrum of gravity waves, while the SOR Na flux excludes the effects of the longer period waves, viz. waves with periods exceeding the mean observation period of  $\sim 7.6$  hr.

Recently, Guo and Liu (2021) reported seasonal variations of the vertical gravity wave heat flux at Cerro Pachón, Chile (CP, 30°S). The measured sensible heat flux reveals strong annual and weak semi-annual oscillations, with the maximum downward fluxes observed in mid-winter during June and July. The heat flux profile exhibits a broad maximum in late June extending from about 88 to 94 km with values averaging about  $-2.5 \text{ Kms}^{-1}$ , similar to the peak value observed in late May at McMurdo. In contrast, observations at Hefei, China (31.5°N) in the fall, revealed a maximum downward heat flux at 88 km of only  $-0.3 \text{ Kms}^{-1}$  and maximum downward Na flux at 89 km of only  $-0.3 \times 10^4 \text{ cm}^{-2} \text{ s}^{-1}$  (Tao Li, private communication, University of Science and Technology of China). These small flux values may reflect significant differences in wave activity at Hefei compared to SOR and CP, and as we will show later, may also be related to temporal resolution with which the data were acquired. Heat and Na flux measurements were also made at Maui, HI (20.7°N). The annual mean heat flux profile exhibited two downward maxima of  $-1.25 \text{ Kms}^{-1}$  at 87 km and  $-1.4 \text{ Kms}^{-1}$  at 95 km. The annual mean Na flux exhibited a downward maximum of  $-0.8 \times 10^4 \text{ cm}^{-2} \text{ s}^{-1}$  at 87 km. Finally, Na flux observations at Table Mt., CO (40°N, Huang et al., 2015) in Aug and Sep (corresponds to Feb and Mar at McMurdo) had a peak value at 86 km of  $-1.5 \times 10^4 \text{ cm}^{-2} \text{ s}^{-1}$ . In summary, the McMurdo heat and Na fluxes reach their maximum downward

values  $\sim 4$  km lower in altitude than the mid-latitude observations. The peak value of heat flux at McMurdo is comparable to the largest values observed at SOR and Cerro Pachón, while the peak Na flux value is the largest by about a factor of 2.

Between 95 and 106 km the heat flux at McMurdo is positive, which suggests that wave dissipation is relatively weak at these higher altitudes near the mesopause where the atmosphere becomes more stable as the environmental lapse rate decreases to zero at the mesopause (102.4 km) and then becomes negative in the lower thermosphere. By comparison, the heat flux is also positive in the thermosphere at SOR above 95 km from April through October when the mesopause is located near 86 km (Chu et al., 2005), reaching values of +1 Km/s near 100 km (Gardner & Liu, 2007). Because the McMurdo heat flux measurements are the first to be reported from above 100 km, there are no other observations in this region and so we compare the measurements with theory.

Wave dissipation can be quantified by calculating the potential temperature flux,

$$\frac{\overline{w'\theta'}}{\theta} = \frac{\overline{w'T'}}{T} - \kappa \frac{\overline{w'p'}}{p} = -\frac{1}{\theta} \frac{\partial \overline{\theta}}{\partial z} K_H \quad (2)$$

where potential temperature  $\theta = T \left( \frac{p_0}{p} \right)^\kappa$ ,  $\kappa = R/C_p$ ,  $R = 287 \text{ m}^2 \text{ K}^{-1} \text{ s}^{-2}$  is the gas constant for dry air,  $C_p = 1,003 \text{ m}^2 \text{ K}^{-1} \text{ s}^{-2}$  is the specific heat at constant pressure,  $p$  is the atmospheric pressure, and  $\overline{w'p'}$  is the gravity wave energy flux. The right-hand-side of Equation 2 follows by invoking Fick's First Law of Diffusion of  $\theta$ , where in this case  $K_H$  is the effective thermal diffusivity induced by non-breaking wave motions. By solving Equation 2 for  $\overline{w'T'}$  and noting that  $\frac{1}{\theta} \frac{\partial \overline{\theta}}{\partial z} = \frac{N^2}{g}$ , we obtain

$$\overline{w'T'} = \left( \Gamma_{\text{ad}} + \partial \overline{T} / \partial z \right) (K_E - K_H), \quad (3)$$

where for convenience we define  $K_E$  as the effective diffusivity associated with the gravity wave energy flux  $\overline{w'p'}$

$$K_E = \kappa \frac{g}{N^2} \frac{\overline{w'p'}}{p}. \quad (4)$$

Potential temperature is a conserved quantity for an air parcel in adiabatic motion, that is, for motion in which there are no heat sources or sinks. Although we believe that this condition may be violated in the lower thermosphere above McMurdo, for the moment let us assume that adiabatic motion applies. We also assume that in the absence of wave dissipation, the wave-induced potential temperature flux and  $K_H$  are zero. In this case, according to Equation 3, the sensible heat flux is proportional to  $K_E$  and the energy flux ( $\overline{w'p'} = \frac{N^2 \overline{p}}{gk} K_E$ ), which is positive for regions dominated by upward-propagating gravity waves. At 103 km, where the positive sensible heat flux at McMurdo reaches  $5.5 \pm 1.5 \text{ Km/s}$ , if  $K_H \simeq 0$  then  $K_E = 580 \pm 160 \text{ m}^2/\text{s}$  and  $\overline{w'p'} = 2.2 \pm 0.6 \text{ mW/m}^2$ . In the following section we show that these large values for  $K_E$  and  $\overline{w'p'}$  are possible according to the gravity wave polarizations relations (Vadas, 2013), especially when the wave spectrum is dominated by upward-propagating waves with the amplitudes and phase speeds that are commonly observed in the lower thermosphere. However, we believe that there may be other factors involved, which could potentially lead to negative values for  $K_H$  and large positive values for the sensible heat flux. These factors include the amplification of inertial period waves, which has been observed for tides and planetary waves in this region above McMurdo (Fong et al., 2014, 2015; Lu, Chu, Chen, et al., 2017). Additionally, heat sources associated with the aurora in the lower thermosphere, may also affect the phase shift between  $w'$  and  $T'$ , which could lead to large positive heat flux values. Coupled with the severe dissipation of primary gravity waves around 85–95 km, the observed profile of sensible heat flux transitioning from downward below 90 km to upward from 97 to 106 km can be explained in terms of the generation of secondary gravity waves and the gravity wave polarization relations. The comparison of the measured heat flux with theory is detailed in Section 5 and the impact of secondary waves is further examined in Section 6.

## 5. Comparison of the Measured Heat and Estimated Energy Fluxes With Theory

The large positive sensible heat flux from 97 to 106.5 km differs from the conventional understanding of wave-driven atmospheric motions, in which the sensible heat flux induced by gravity waves is expected to be either zero for conservative waves or negative for dissipating waves regardless of the wave propagation direction

(Walterscheid, 1981). Although we focus here on the late May 2020 observations, we have observed positive sensible heat fluxes in the lower thermosphere on numerous other winter days, however the magnitudes vary. Positive heat fluxes appears to be a common feature of the lower thermosphere in winter above McMurdo. As shown in Appendix C, the heat and energy fluxes can be directly calculated from the gravity wave polarization relations. For our analysis we employ the compressible, f-plane, non-dissipative polarization relations for  $w'$ ,  $T'$  and  $p'$  given by Equations B11 and B7 in Vadas (2013).

### 5.1. Expected Heat and Energy Fluxes From Polarization Relations

For gravity wave oscillations of the form  $\exp[i(\omega_r t - kx - ly - mz - \phi)]$ , the heat and energy fluxes, for an individual wave with ground-based frequency  $\omega_r$ , intrinsic frequency  $\omega$ , and zonal, meridional and vertical wave-numbers of  $k$ ,  $l$ , and  $m$ , are given by (see Appendix C)

$$\overline{w'(t)T'(t)} = \frac{1}{2} A_w A_T \cos(\phi_w - \phi_T) = -\frac{(\gamma-1)}{2\gamma H} \frac{g}{N^2} \frac{A_T^2}{\overline{T}} \frac{\frac{\omega}{m} \left(1 - \frac{\omega^2}{N^2}\right)}{\left[1 + \frac{1}{(mH)^2} \left(\frac{1}{2} - \frac{\gamma-1}{\gamma} \frac{\omega^2}{N^2}\right)^2\right]} \quad (5)$$

and

$$\overline{w'(t)p'(t)} = \frac{1}{2} A_w A_p \cos(\phi_w - \phi_p) = -\frac{\bar{\rho} g^2}{2N^2} \frac{A_T^2}{\overline{T}^2} \frac{\frac{\omega}{m} \left(1 - \frac{\omega^2}{N^2}\right)}{\left[1 + \frac{1}{(mH)^2} \left(\frac{1}{2} - \frac{\gamma-1}{\gamma} \frac{\omega^2}{N^2}\right)^2\right]}, \quad (6)$$

where  $A_w$ ,  $A_T$ , and  $A_p$  are the wave amplitudes in  $w'$ ,  $T'$ , and  $p'$ , and  $\phi_w$ ,  $\phi_T$ , and  $\phi_p$  are the phases for the maximum fluctuations.  $\gamma = C_p/C_v \approx 1.4$  for  $z \sim 100$  km. The phase differences are

$$\phi_w - \phi_T = \frac{\pi}{2} + \tan^{-1} \left[ \frac{1}{mH} \left( \frac{1}{2} - \frac{1}{\gamma} \right) \right] + \tan^{-1} \left[ \frac{1}{mH} \left( \frac{1}{2} - \frac{\gamma-1}{\gamma} \frac{\omega^2}{N^2} \right) \right] \quad (7)$$

and

$$\phi_w - \phi_p = \pi + \tan^{-1} \left[ \frac{\gamma-2}{2\gamma mH} \right]. \quad (8)$$

Note that for these equations,  $m$  is negative (positive) for upward (downward) propagating waves. These are exact equations which follow from the polarizations relations (Vadas, 2013). Because  $w'$  and  $T'$  are nearly  $90^\circ$  out of phase, the sensible heat flux is especially sensitive to the phase difference between these two parameters. In contrast, because  $w'$  and  $p'$  are nearly  $180^\circ$  out of phase, the energy flux is insensitive to the phase difference.

To facilitate the discussion below, we rewrite the polarization relation Equation C4 here:

$$w' = \frac{-ig\omega}{N^2} \frac{\left[1 - \frac{i}{mH} \left(\frac{1}{2} - \frac{1}{\gamma}\right)\right]}{\left[1 + \frac{i}{mH} \left(\frac{1}{2} - \frac{\gamma-1}{\gamma} \frac{\omega^2}{N^2}\right)\right]} \frac{T'}{\overline{T}}. \quad (9)$$

Equation 7 is derived directly from this full polarization relation and shows that the phase difference between  $w'$  and  $T'$  differs from  $90^\circ$ . That is,  $\phi_w - \phi_T < 90^\circ$  for an upward-propagating, non-dissipative gravity wave with  $\omega < N$ , and  $\phi_w - \phi_T > 90^\circ$  for a downward-propagating wave with  $\omega < N$ . Consequently, the sensible heat flux is expected to be positive and negative for upward and downward propagating waves, respectively.

Many researchers employ the Boussinesq approximation ( $1 \ll 2mH$ ) directly to the polarization relation Equation 9 in their analyses:  $w' \simeq \frac{-ig\omega}{N^2} \frac{T'}{\overline{T}}$ . In this case the phase difference between  $w'$  and  $T'$  is exactly  $90^\circ$  (also see Equation B18 in Vadas, 2013), that is, the last two terms in Equation 7 are neglected, and so the sensible heat flux  $\overline{w'T'}$  is assumed to be zero for non-dissipating waves regardless of their propagation direction. However, applying the Boussinesq assumption directly to the polarization relations without distinguishing between the magnitude



and phase of the wave fluctuations, is invalid in the MLT as shown by the right-hand-side of Equations 5 and by 9. Instead, applying the Boussinesq approximation to the exact expression for the heat flux (but not to the polarization relations) is valid and we obtain

$$\overline{w'(t)T'(t)} \simeq -\frac{1}{2} \frac{g^2 A_T^2}{C_p N^2 (\bar{T})^2} \frac{\omega}{m} \left(1 - \frac{\omega^2}{N^2}\right) \simeq -\frac{A_T^2}{2\bar{T}} \frac{\omega}{m}, \quad (10)$$

where we note that  $\frac{\gamma-1}{\gamma} = \frac{R}{C_p}$  and  $H = \bar{RT}/g$ . For upward propagating, non-dissipating waves where  $m$  is negative, the actual heat flux is positive, not zero, even under the Boussinesq approximation.

Upward-propagating gravity waves with fast vertical phase speeds ( $-\omega/m$ ) and relatively large temperature amplitudes ( $A_T$ ) or with slow phase speeds but large temperature amplitudes, can induce large, positive, sensible heat fluxes. In fact, the sensible heat flux can be quite large and positive in the lower mesosphere at McMurdo where dissipation is weak and mesoscale ( $\sim 15$ – $30$  km) vertical wavelength waves are common (e.g., Chen & Chu, 2017; Chen et al., 2016; Chu, Yu, et al., 2011). For example, for a vertical wavelength of 20 km and an intrinsic period of 16.7 min, the intrinsic vertical phase speed ( $\omega/m$ ) is 20 m/s. The mean temperature was about 175 K at 103 km at McMurdo during our observations, so if the temperature amplitude of the upward-propagating wave is 5 K, then the wave would induce a positive heat flux of about  $+1.4 \text{ Kms}^{-1}$ . According to Equation 7 this corresponds to a phase shift of about  $-8.6^\circ$  from  $90^\circ$ . For persistent gravity waves at McMurdo (Chen et al., 2016), the typical vertical wavelength and period are 20 km and 5 hr, respectively, so the corresponding vertical phase speed is  $\sim 1.1 \text{ m/s}$ . These lower frequency waves usually have very large amplitudes  $\sim 20 \text{ K}$  at 105 km, so they can contribute positive heat fluxes  $\sim +1.2 \text{ Kms}^{-1}$ , which is comparable to the contribution from the high-frequency waves. If there are on average 3–5 upward-propagating waves present simultaneously in the lower thermosphere at McMurdo with these average characteristics, then the total heat flux would be  $+4$  to  $+6 \text{ Kms}^{-1}$ , similar to the values observed. This exercise demonstrates that the predicted phase shift between  $w'$  and  $T'$  of  $\sim 8$ – $9^\circ$  less than  $90^\circ$  can lead to large, positive sensible heat fluxes induced by upward-propagating, non-dissipating gravity waves with vertical wavelengths  $\sim 20$  km.

The phase difference between  $w'$  and  $T'$  predicted above from the polarization relations given in Vadas (2013) are supported by lidar observations of vertical winds and temperatures over Boulder, Colorado (Lu, Chu, Li, et al., 2017). Lu, Chu, Li, et al. (2017) measured the phase differences between  $w'$  and  $T'$  for 184 mesoscale waves observed between 85 and 100 km at Table Mt., CO. They found that the mean phase difference  $\phi_w - \phi_T = 84.2^\circ$  was  $2.6^\circ$  larger than the phase difference  $81.6^\circ$  predicted by Equation 7, which they showed was likely caused by dissipation associated with damping by eddy and molecular viscosity (Lu, Chu, Li, et al., 2017). To compute the potential temperature  $\theta$  flux from the polarization relations, we add additional phase shifts  $\Delta\phi_{w'T'}$  and  $\Delta\phi_{w'p'}$  to the phase differences between  $w'$  and  $T'$  and between  $w'$  and  $p'$  to account for dissipation and other effects. As shown in Appendix C, we have

$$\overline{w'\theta'} = \bar{\theta} \left( \frac{\overline{w'T'}}{\bar{T}} - \frac{R}{C_p} \frac{\overline{w'p'}}{\bar{p}} \right) \simeq -\frac{g\omega\bar{\theta}}{2N^2} \frac{A_T^2}{\bar{T}^2} \sin(\Delta\phi_{w'T'}). \quad (11)$$

The small phase shifts between  $w'$  and  $p'$  caused by dissipation and other effects are negligible because these fluctuations are nearly  $180^\circ$  out of phase. In contrast, the small phase shifts between  $w'$  and  $T'$  are significant because these fluctuations are approximately  $90^\circ$  out of phase. If there is no dissipation  $\Delta\phi_{w'T'} = 0$ , the contributions from heat flux and energy flux in Equation 11 cancel each other (see Appendix C for details) and  $\overline{w'\theta'} = 0$ . But  $\overline{w'T'}$  can be positive or negative depending on the direction of wave propagation, according to Equation 10. If there is dissipation  $\Delta\phi_{w'T'} > 0$  as shown by the Boulder, CO observations (Lu, Chu, Li, et al., 2017),  $\overline{w'\theta'}$  is negative and again,  $\overline{w'T'}$  can be positive or negative depending on the direction of wave propagation and the value of  $\Delta\phi_{w'T'}$ . This result differs from that of Walterscheid (1981), who concluded that dissipating gravity waves must always exhibit a downward sensible heat flux regardless of the wave propagation direction. Notice also, if  $\Delta\phi_{w'T'}$  is negative, which we speculate may occur if heat sources are present or the wave is amplified, the positive sensible heat flux would be even larger. Then according to Equation 11,  $\overline{w'\theta'}$  could also be positive. This possibility is discussed in Section 7.3.

## 5.2. Estimation of $K_E$ and $K_H$ From Gravity Wave Spectrum

The energy flux and  $K_E$  can be derived in terms of the joint vertical wavenumber ( $m$ ) and intrinsic frequency ( $\omega$ ) spectrum of the gravity wave temperature fluctuations (Gardner, 2018; Liu, 2009). Equations 5, 6 and 11, which apply to individual gravity waves, are easily modified to represent the impact of a spectrum of waves by replacing  $A_T^2/2$  by  $F_{T'}(m, \omega)dm d\omega/(2\pi)^2$ , where  $F_{T'}$  is the 2-D  $(m, \omega)$ -spectrum of the temperature fluctuations, and integrating over  $m$  and  $\omega$ . The energy flux, or equivalently  $K_E$ , is derived in Appendix A by employing a model spectrum for  $F_{T'}$  and assuming that the spectra of upward and downward propagating waves are identical

$$K_E \simeq (1 - 2\alpha_{\text{down}}) \beta(s, q) \frac{\Gamma_{\text{ad}} f}{\bar{T} \sqrt{\xi_{\text{inst}}}} \left[ \frac{\text{Var}(T')}{(\Gamma_{\text{ad}} + \partial \bar{T} / \partial z)^2} \right]^{3/2}, \quad (12)$$

where  $\xi_{\text{inst}}$  is the normalized lapse rate variance, also called the instability parameter (see Equation A9),  $\alpha_{\text{down}}$  is the fraction of wave energy that is propagating downward, and  $\beta$  is a dimensionless parameter that describes the distribution of wave energy versus  $m$  and  $\omega$  (see Equation A7).

$$\beta(s, q) = \begin{cases} \frac{2(s+1)}{s} \sqrt{\frac{(s+1) \ln(N/f)}{(s+3)}} (1 - \sqrt{f/N}) & \text{for } q = 2 \\ \frac{(s+1)}{2s} \sqrt{\frac{(s+1)(\sqrt{N/f} - 1)}{(s+3)}} \ln(N/f) & \text{for } q = 3/2 \\ \frac{(s+1)(q-1)}{s(q-3/2)} \sqrt{\frac{(s+1)(q-1)[(N/f)^{2-q} - 1]}{(s+3)(2-q)}} [1 - (f/N)^{q-3/2}] & \text{for } q \neq 2 \text{ or } 3/2 \end{cases} \quad (13)$$

The parameters  $s$  and  $q$  are characteristics of the spectrum model. For this model the 1-D intrinsic  $\omega$ -spectrum is proportional to  $\omega^{-q}$  and the 1-D  $m$ -spectrum is proportional to  $m^s$  for  $0 \leq m \leq m_*$  and  $m^{-2q+1}$  for  $m_* \leq m$ , where  $m_*$  is the characteristic vertical wavenumber given by Equation A4. Although observations have shown that these parameters can vary, the nominal values are usually assumed to be  $s = 1$  and  $q = 2$ . The nominal value  $q = 2$  is consistent with the wide body of measured spectra in the stratosphere and mesosphere, although observations do suggest that  $q$  decreases as the latitude increases (Allen & Vincent, 1995; Pfenninger et al., 1999). The energy flux is roughly proportional to the mean vertical phase speed of the waves so that for  $0 < s < 1$  and  $0 < q < 2$ , the magnitude of the energy flux is larger, because the spectrum includes faster, vertically propagating waves, than for  $s = 1$  and  $q = 2$ . It is important to note that this expression was derived by assuming that the joint vertical wavenumber ( $m$ ) and temporal frequency ( $\omega$ ) spectrum of the downward waves is proportional to the spectrum of the upwardly propagating waves, that is, only the spectrum magnitudes are different. It is clear from Equation 12 that if most waves propagate upward ( $\alpha_{\text{down}} < 0.5$ ),  $K_E$  and the energy flux will be positive (upward). However,  $K_E$  can be negative at some altitudes if the majority of the wave energy is propagating downward. This might occur, for example, in a region of strong primary wave dissipation and subsequent strong secondary wave generation.

Similarly, by combining Equations 2 and 11, we obtain

$$K_H \simeq \frac{f}{(\Gamma_{\text{ad}} + \partial \bar{T} / \partial z)^2} \frac{1}{(2\pi)^2} \int d\omega \int dm \sin[\Delta\phi_{w'T'}(m, \omega)] \frac{\omega}{f} F_{T'}(m, \omega) = \epsilon(q) \frac{f \text{Var}(T') \overline{\sin(\Delta\phi_{w'T'})}}{(\Gamma_{\text{ad}} + \partial \bar{T} / \partial z)^2} \quad (14)$$

where

$$\epsilon(q) = \begin{cases} \ln\left(\frac{N}{f}\right) & \text{for } q = 2 \\ \frac{(q-1)}{(2-q)} \left[ \left(\frac{N}{f}\right)^{2-q} - 1 \right] & \text{for } q \neq 2 \end{cases} \quad (15)$$

and

$$\overline{\sin(\Delta\phi_{w'T'})} = \exp[-\text{Var}(\Delta\phi_{w'T'})/2] \sin\left(\overline{\Delta\phi_{w'T'}}\right). \quad (16)$$

Note in Equation 14,  $\overline{\sin(\Delta\phi_{w'T'})}$  represents the sample mean, which is computed with respect to the distribution of wave energy versus  $m$  and  $\omega$ . We assume that many statistically independent waves comprise the wave spectrum so that  $\Delta\phi_{w'T'}$  is approximately Gaussian distributed, which leads to Equation 16. Since we do not know theoretically how  $\Delta\phi_{w'T'}$  varies with  $m$  and  $\omega$ , this is the best that we can do. However, if we can estimate  $K_H$  using the observed data, then Equations 14 and 16 can be used to determine the mean phase shift associated with dissipation and other effects. For the Lu, Chu, Li, et al. (2017) data set, the mean phase shift associated with dissipation was  $+2.6^\circ$  and the standard deviation was  $26.7^\circ$ , so that  $\sin(\Delta\phi_{w'T'}) \simeq 0.04$ . If these wave dissipation statistics apply approximately to the McMurdo data set, and the waves in the lower thermosphere at McMurdo are experiencing dissipation similar to the waves observed between 85 and 100 km at Boulder, CO, then according to Equation 14 we find that  $K_H \simeq 54 \text{ m}^2/\text{s}$  for  $q = 2$  and  $K_H \simeq 120 \text{ m}^2/\text{s}$  for  $q = 3/2$ .

As we demonstrated for individual waves of the type encountered in the MLT at McMurdo, it is possible for a spectrum of waves to induce the large positive heat flux observed at 103 km. If we assume there is no dissipation and  $K_H = 0$ , then by applying Equations 3 and 12 with  $K_E = \frac{w'T'}{\Gamma_{ad} + \partial T/\partial z} \approx 580 \text{ m}^2/\text{s}$ , we find that  $(1 - 2\alpha_{\text{down}}) \cdot \beta(s, q) = 19.8$ , which is achieved if  $\alpha_{\text{down}} = 0$ ,  $s = 0.37$ , and  $q = 3/2$ . This wave spectrum model exhibits more energy at the larger vertical wavelengths and higher frequencies than the nominal  $s = 1$  and  $q = 2$  model, which increases the mean phase speed leading to a much larger positive heat flux. Conversely, if we assume a nominal spectrum dominated by upward-propagating waves ( $\alpha_{\text{down}} = 0$ ) with  $s = 1$  and  $q = 2$ , then  $K_E = 170 \text{ m}^2/\text{s}$  and according to Equation 3,  $K_H \simeq -410 \text{ m}^2/\text{s}$ . Recall that  $K_H$  is the effective wave-induced thermal diffusivity. Although the cumulative motions arising from a spectrum of waves appear random, in reality each individual wave imparts an organized motion to the atmosphere. An upward-propagating spectrum of waves imparts an upward Stokes drift to the atmosphere which can transport constituents and potential temperature against their density gradients. Thus, for organized wave motions,  $K_H$  can be negative. If  $K_H = -410 \text{ m}^2/\text{s}$  when  $q = 2$ , then  $\overline{\Delta\phi_{w'T'}} \simeq -18^\circ$ , and if  $K_H = -306 \text{ m}^2/\text{s}$  when  $q = 5/3$ , then  $\overline{\Delta\phi_{w'T'}} \simeq -7.6^\circ$ , according to Equation 14. These additional phase shifts are comparable to the  $-8.4^\circ$  phase shift from  $90^\circ$  predicted by Equation 7 for non-dissipating, upward-propagating waves with vertical wavelengths averaging 20 km, and the  $+2.6^\circ$  measured by Lu, Chu, Li, et al. (2017) caused by dissipation of the mesopause region waves they observed at Boulder, CO. These examples demonstrate the importance of the wave spectral characteristics, including  $\alpha_{\text{down}}$ , in determining the sensible heat, potential temperature, and energy fluxes and their associated diffusivities. The large positive heat flux in the thermosphere is certainly consistent with theory. However, it is not clear whether this result arises largely because of changes in the wave spectrum or because  $K_H$  is negative due to phase shifts induced by effects like in-situ heat sources or perhaps, wave amplification. In Section 6 we gain additional insight about  $K_H$  and  $K_E$  by comparing the measured Na and sensible heat fluxes with theory.

### 5.3. Sensible Heat Flux Profile

The strong dissipation of primary gravity waves before reaching the  $E_{\text{pm}}$  peak around 86 km (see Figure 4 and discussion in Section 3) leads to a phase shift  $\Delta\phi_{w'T'} \gg 0$  thus  $\phi_w - \phi_T \gg 90^\circ$ , resulting in the negative (downward) sensible heat flux as observed. The  $w'T'$  negative peak altitude of  $\sim 84$  km is determined by the competition between the phase difference and wave amplitudes in  $w'$  and  $T'$ , coupled with the strong downwelling in winter at McMurdo. Severe damping (breaking and cascading to turbulence plus deposition of momentum) of primary waves above the  $E_{\text{pm}}$  peak leads to the generation of secondary gravity waves that propagate both upward and downward (Vadas & Becker, 2019; Vadas et al., 2018). The nearly zero heat flux between 90 and 95 km is a result of the associated upward and downward fluxes balancing each other, coupled with the initial small amplitudes of the secondary waves (as well as surviving primary waves) that are experiencing little dissipation.

The upward-propagating mesoscale secondary gravity waves experience little dissipation from 97 to 102 km as indicated by the  $E_{\text{pm}}$  profile and its inverse scale height in Figure 4. Therefore, the wave amplitudes in  $w'$  and  $T'$  grow with decreasing atmospheric density while the phase difference  $\phi_w - \phi_T$  remains below  $90^\circ$  (due to the negligible additional phase shift  $\Delta\phi_{w'T'} \sim 0$ ), resulting in the increasingly positive sensible heat flux with a peak at  $\sim 103$  km, according to Equation 5. The  $E_{\text{pm}}$  growth slows down above 103 km, indicating appreciable dissipation of the secondary waves. The additional phase shift  $\Delta\phi_{w'T'}$  associated with dissipation becomes increasingly positive, making the phase difference  $\phi_w - \phi_T$  approach  $90^\circ$ . Thus, the positive sensible heat flux starts to decrease in magnitude above 103 km as observed. When the secondary waves experience severe damping or breaking (as indicated by the second peak of  $E_{\text{pm}}$  around 112 km), the phase difference  $\phi_w - \phi_T$  will exceed  $90^\circ$ .

and result in negative (downward) sensible heat flux again. Unfortunately, the current lidar data signal-to-noise ratio (SNR) does not allow the unambiguous determination of  $\overline{w'T'}$  above 106 km.

Overall, the profiles of  $\overline{w'T'}$ ,  $E_{\text{pm}}$ , and inverse scale heights along with the variances in Figure 3 convey a coherent story of heat transport in the MLT by primary and secondary gravity waves via multistep vertical coupling. The impact of these waves on the constituent transport is examined in Section 6. Furthermore, wave amplification and heat sources, if any, could also contribute to the positive  $\overline{w'T'}$ . This possibility is discussed in Section 7.3.

## 6. Comparison of the Measured Na Flux With Theory

Atmospheric constituents can be transported vertically by five different mechanisms: (a) advection, (b) molecular diffusion, (c) eddy diffusion by turbulence, (d) atmospheric mixing by non-breaking waves, and (e) chemical transport by waves and turbulence. Our observations of the Na flux only include mechanisms (d) and (e), viz. the effects of wave mixing and chemical transport caused by wave perturbations in Na chemistry. The theoretical expression for the vertical constituent flux of a chemically active species C, induced by non-breaking gravity waves is given by Equations 1–4 in Gardner et al. (2019) by simply setting the eddy and molecular diffusivities to zero and multiplying the transport velocities by the species density.

$$\overline{w'\rho_C'} = \bar{\rho}_C \frac{\overline{w'\rho_A'}}{\bar{\rho}_A} - \bar{\rho}_C \left( \frac{g}{RT} + \frac{1}{T} \frac{\partial \bar{T}}{\partial z} + \frac{1}{\bar{\rho}_C} \frac{\partial \bar{\rho}_C}{\partial z} \right) K_{\text{Wave}} + \overline{w'\rho_C'}_{\text{Chemical}} \quad (17)$$

The parameters  $\rho_A$  and  $\rho_C$  are the atmospheric and constituent number densities. The first term on the right-hand-side of the (Equation 16) is the contribution from the vertical Stokes drift imparted to the atmosphere by the gravity waves (e.g., Coy et al., 1986; Walterscheid & Hocking, 1991). The second term is caused by mixing of the atmosphere by the spectrum of non-breaking waves. Although this term has the form of classical diffusion, as discussed below it is fundamentally different than eddy and molecular diffusion. The third term is the chemical flux which arises from wave-induced perturbations in the constituent chemistry that are partially correlated with the vertical wind fluctuations (Gardner & Liu, 2016).  $K_{\text{Wave}} = \overline{w'\zeta}$  is the effective wave diffusivity associated with the wave-induced vertical displacement fluctuations, which we denote by  $\zeta$  (Gardner, 2018).  $K_{\text{Wave}}$  is also related to the Stokes drift velocity (Gardner et al., 2019) and to  $K_H$  and  $K_E$

$$K_{\text{Wave}} = \frac{g}{N^2} \frac{\overline{w'\rho_A'}}{\bar{\rho}_A} = -\frac{g}{N^2} \left( \frac{\overline{w'T'}}{\bar{T}} - \frac{\overline{w'p'}}{\bar{p}} \right) = K_H + \left( \frac{C_p}{R} - 1 \right) K_E. \quad (18)$$

This expression on the right-hand-side of Equation 18 for  $K_{\text{Wave}}$  is valid provided each individual wave in the spectrum obeys the gravity wave polarization and dispersion relations and  $\frac{\text{Var}(\rho_A')}{\bar{\rho}_A^2} \sim \frac{\text{Var}(T')}{\bar{T}^2} \ll 1$ , which is easily satisfied throughout the MLT above McMurdo. By combining Equations 17 and 18, the constituent flux can also be written as

$$\overline{w'\rho_C'} \simeq -\bar{\rho}_C \left( \frac{g}{RT} - \frac{g}{C_p \bar{T}} + \frac{1}{\bar{\rho}_C} \frac{\partial \bar{\rho}_C}{\partial z} \right) K_{\text{Wave}} + \overline{w'\rho_C'}_{\text{Chemical}}. \quad (19)$$

Although  $K_{\text{Wave}}$  has units of diffusivity, atmospheric mixing caused by non-breaking waves is fundamentally different than classical eddy and molecular diffusion because of the Stokes drift term and the nature of the organized motion induced by waves. The vertical temperature gradient  $\partial \bar{T} / \partial z$  in the classical diffusion term in Equation 17 is replaced by  $-g/C_p = -\Gamma_{\text{ad}}$  in the wave mixing term in Equation 19. This change can have a significant impact on the constituent flux profile and our interpretation of  $K_{\text{Wave}}$ , especially in the thermosphere where  $\partial \bar{T} / \partial z$  is positive but  $-g/C_p$  is negative.  $K_{\text{Wave}}$  arises through the atmospheric mixing induced by the spectrum of propagating waves, which is different than the mixing associated with the random velocity fluctuations caused by turbulence or the random thermal motions of atmospheric molecules. Each wave imparts an organized, non-random motion to the atmosphere even though the cumulative effect of the wave spectrum appears random. While molecular and eddy diffusivities are always positive,  $K_{\text{Wave}}$  can be negative in regions where the wave spectrum is dominated by downward propagating waves so that the Stokes drift is downward. And, as pointed out in the previous section, the wave-induced thermal diffusivity  $K_H$ , associated with the potential temperature flux,



can also be negative. For this reason, we refer to the constituent (and heat) transport caused by this non-random wave mixing as wave transport to distinguish it from eddy transport caused by the random atmospheric mixing imparted by turbulence.

### 6.1. Deriving $K_{\text{Wave}}$ , $K_H$ , and $K_E$ From Measured Fluxes

The  $K_{\text{Wave}}$ ,  $K_H$ , and  $K_E$  profiles can be derived in terms of the measured heat and Na fluxes by combining Equations 3, 18, and 19 as

$$K_{\text{Wave}} = - \frac{\left( \overline{w' \rho'_C} - \overline{w' \rho'_{C\text{Chemical}}} \right)}{\bar{\rho}_C \left( \frac{g}{RT} - \frac{g}{C_p T} + \frac{1}{\bar{\rho}_C} \frac{\partial \bar{\rho}_C}{\partial z} \right)} \quad (20a)$$

$$K_H = - \left( 1 - \frac{R}{C_p} \right) \frac{\overline{w' T'}}{\left( \Gamma_{\text{ad}} + \frac{\partial \bar{T}}{\partial z} \right)} + \frac{R}{C_p} K_{\text{Wave}} \quad (20b)$$

$$K_E = \frac{R}{C_p} \frac{\overline{w' T'}}{\left( \Gamma_{\text{ad}} + \frac{\partial \bar{T}}{\partial z} \right)} + \frac{R}{C_p} K_{\text{Wave}} \quad (20c)$$

Taking into account the measurement uncertainties of Na and heat fluxes, we estimate the uncertainties of the derived  $K_{\text{Wave}}$ ,  $K_H$ , and  $K_E$  as

$$(\Delta K_{\text{Wave}})_{\text{rms}} = \frac{\left( \Delta \overline{w' \rho'_{\text{Na}}} \right)_{\text{rms}}}{\left| \bar{\rho}_C \left( \frac{g}{RT} - \frac{g}{C_p T} + \frac{1}{\bar{\rho}_C} \frac{\partial \bar{\rho}_C}{\partial z} \right) \right|} \quad (21a)$$

$$(\Delta K_H)_{\text{rms}} = \sqrt{\left( 1 - \frac{R}{C_p} \right)^2 \frac{\text{Var}(\Delta \overline{w' T'})}{\left( \Gamma_{\text{ad}} + \frac{\partial \bar{T}}{\partial z} \right)^2} + \left( \frac{R}{C_p} \right)^2 \text{Var}(\Delta K_{\text{Wave}})} \quad (21b)$$

$$(\Delta K_E)_{\text{rms}} = \sqrt{\left( \frac{R}{C_p} \right)^2 \frac{\text{Var}(\Delta \overline{w' T'})}{\left( \Gamma_{\text{ad}} + \frac{\partial \bar{T}}{\partial z} \right)^2} + \left( \frac{R}{C_p} \right)^2 \text{Var}(\Delta K_{\text{Wave}})} \quad (21c)$$

To apply the equations in Equation 20, we computed the chemical flux (see Section 6.3 for details) and subtracted it from the measured Na flux profile before deriving the three diffusivities. The denominator of the Na flux term goes to zero near 94 km and the uncertainties become quite large. In this region, we linearly interpolated  $K_{\text{Wave}}$  and eliminated the error bars on the diffusivity profiles to denote the interpolated region. The profiles of  $K_{\text{Wave}}$ ,  $K_H$ , and  $K_E$  derived in Equation 20 are plotted, respectively, in Figures 7a, 7b and 7c, along with the eddy diffusivity profile ( $K_{zz}$ ) obtained from the Whole Atmosphere Community Climate model (WACCM, Wuhu Feng, private communication, University of Leeds).

$K_{\text{Wave}}$  and  $K_H$  exhibit their maximum positive values at 84 km (400 m<sup>2</sup>/s and 360 m<sup>2</sup>/s, respectively) where the downward Na and sensible heat fluxes are also maximum (Table 1). This is also the region where wave mixing is large as characterized by the normalized  $\text{Var}(T')$  (Figure 3e) and the atmospheric instability is also large as characterized by the normalized  $\text{Var}(-\partial T'/\partial z)$  (Figure 3f).  $K_{\text{Wave}}$  and  $K_H$  are negative from 89 to 106 km. As mentioned previously, mixing by non-breaking waves is fundamentally different than mixing by the random turbulence and molecular thermal motions. Waves impart organized motions to the atmosphere which, under certain conditions, can lead to upward potential temperature transport and constituent transport against the concentration gradient. In other words, the wave-induced values of  $K_{\text{Wave}}$  and  $K_H$  can be negative, although in most cases they are expected to be positive. The negative values of  $K_{\text{Wave}}$  and  $K_H$  occur in the mesopause region and lower thermosphere where

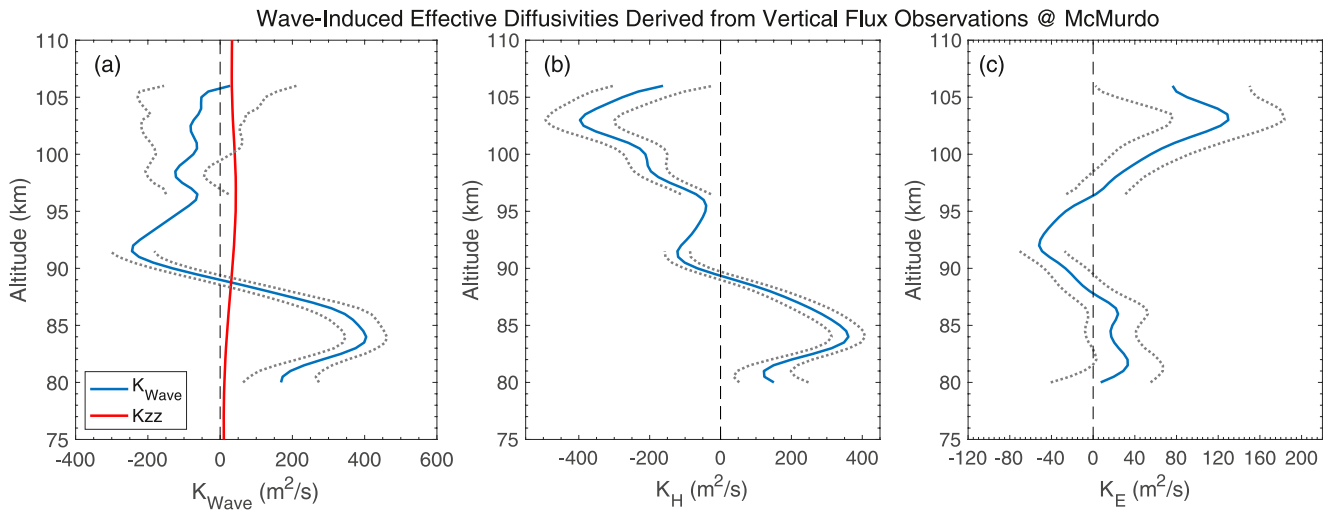


**Figure 7.** Profiles of (a) the effective wave diffusivity ( $K_{\text{Wave}}$ ), (b) the thermal diffusivity ( $K_H$ ), (c) effectivity diffusivity associated with the gravity wave energy flux ( $K_E$ ), derived from the vertical flux observations in the upper mesosphere and lower thermosphere above McMurdo in late May 2020. The red curve in (a) is the eddy diffusivity profile ( $K_{zz}$ ) obtained from WACCM.

we have suggested previously that the wave-induced motions may not be strictly adiabatic because of the presence of heat sources and where there may be amplification of some of the gravity waves. Notice that  $K_E$  becomes negative in the region between about 88 and 96 km, where the Na flux is positive (upward) and the sensible heat flux is near zero. A negative  $K_E$  implies that more than half of the wave energy is propagating downward ( $\alpha_{\text{down}} > 0.5$ , see Equation 12).

## 6.2. Estimation and Analysis of $\alpha_{\text{down}}$

Wave dissipation, reflection, and ducting as well as wave sources vary with altitude. All these factors will affect the population of downward propagating waves, making  $\alpha_{\text{down}}$  altitude dependent. We now apply Equation 12 to gain some insight about  $\alpha_{\text{down}}$  and the spectrum shape parameters  $s$  and  $q$ . The factor  $(1 - 2\alpha_{\text{down}})\beta(s, q)$  can be tuned to produce a theoretical  $K_E$  profile given by Equation 12 that closely matches Equation 20c, the profile derived from the measured Na and sensible heat fluxes. We simplify this approach by adopting the nominal values of  $s = 1$ ,  $q = 2$ , and  $\beta(1, 2) = 5.8$  at McMurdo and then adjust  $\alpha_{\text{down}}$  so that Equation 12 equals Equation 20c. Obviously, this approach only provides an estimate of  $\alpha_{\text{down}}$  because the spectral shape is expected to change with altitude as various waves break, are damped or perhaps are amplified as they propagate through the atmosphere. Because the sign of  $\beta$  is positive, this approach does reveal those regions where more than half the wave energy is propagating downward. The resulting  $\alpha_{\text{down}}$  profile is plotted in Figure 8a. To illustrate the impact of changes in the wave spectrum with altitude, we also derived the  $\alpha_{\text{down}}$  profile for  $s = 1$ ,  $q = 5/3$ , and  $\beta(1, 5/3) = 9.356$  and plotted it in Figure 8b. For  $q = 2$ , the m-spectrum is proportional to  $m^{-3}$  at the highest wavenumbers and for  $q = 5/3$  spectrum is proportional to  $m^{-2.33}$ . Previous studies have shown that the m-spectrum does become more shallow in the stratosphere at the higher latitudes (Allen & Vincent, 1995; Pfenninger et al., 1999). For  $q = 2$ ,  $\alpha_{\text{down}}$  reaches its maximum value of 72% at 92.5 km and for  $q = 5/3$  the maximum value is 64% also at 92.5 km. Of course, the  $\alpha_{\text{down}}$  maxima occur in the region where  $K_{\text{Wave}}$  was interpolated so the uncertainty is large but unknown. However, it is clear from the Na flux and transport velocity profiles (Figures 5b and 6b) and Equation 19, that  $K_{\text{Wave}}$  must be negative between 89 and ~95 km where  $\left(\frac{g}{RT} - \frac{g}{C_p T} + \frac{1}{\rho_{\text{Na}}} \frac{\partial \rho_{\text{Na}}}{\partial z}\right)$  and the Na flux are both positive, while the chemical flux and sensible heat flux are negligible. From Equation 18 we see that the energy flux must also be negative in this same region and that requires  $\alpha_{\text{down}}$  to be larger than 50%. That is, in the region between 89 and 95 km more than 50% of the wave energy must be associated with downward propagating waves, regardless of the shape of the wave spectrum.

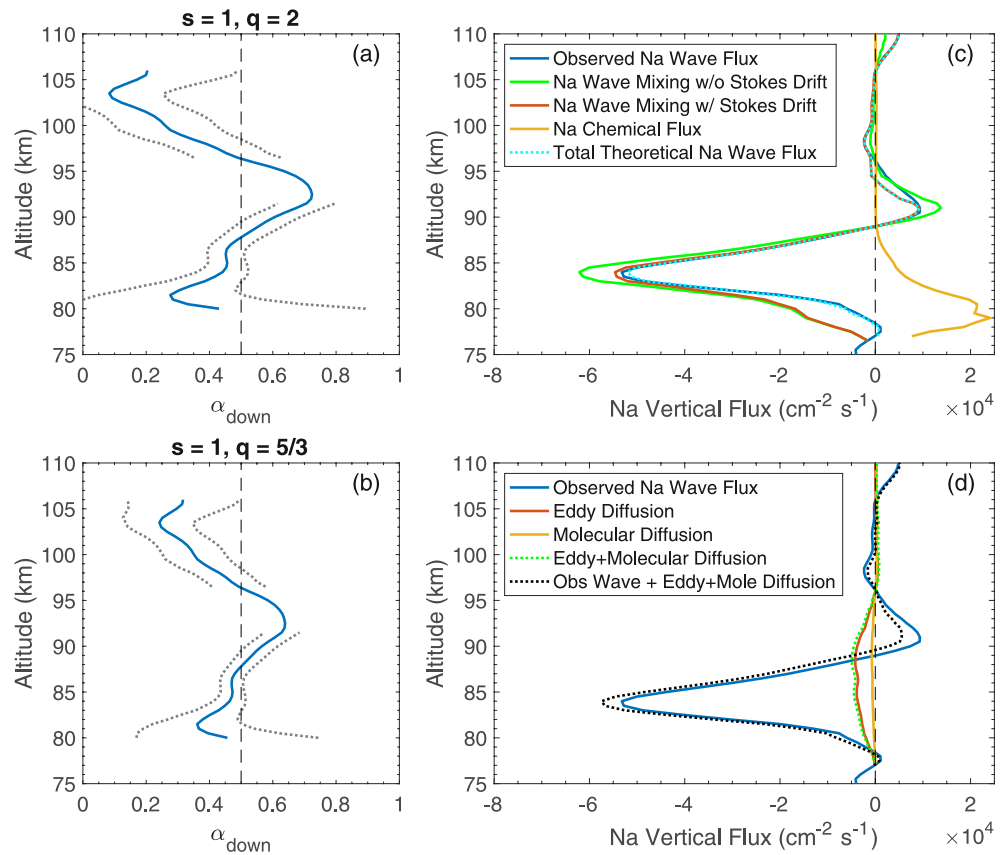


**Figure 8.** Derived altitude profiles of  $\alpha_{\text{down}}$  that provide the best match between the measured and predicted Na and heat flux profiles for (a)  $s = 1, q = 2$  and  $\beta(1,2) = 5.801$  and for (b)  $s = 1, q = 5/3$  and  $\beta(1,5/3) = 9.356$ . (c) Comparison of the directly measured and predicted vertical fluxes of Na, and (d) comparison of observed wave-induced Na flux with the predicted fluxes caused by molecular and eddy diffusion.

Observations and modeling have shown that waves can propagate downward from sources or reflections at higher altitudes or because the waves are propagating in atmospheric ducts (e.g., Walterscheid & Hickey, 2009; Yu & Hickey, 2007). Numerous studies, employing hodograph techniques to unambiguously determine gravity wave propagation directions, have reported extensive observations of  $\alpha_{\text{down}}$  made throughout the atmosphere. These studies have shown that  $\alpha_{\text{down}}$  can vary over a relatively wide range depending on location, altitude, and season. For example, Wang et al. (2005) analyzed extensive balloon sonde measurements over the U.S. and reported that on average  $\sim 50\%$  of the gravity wave energy propagates downward in the troposphere and  $\sim 25\%$  propagates downward in the lower stratosphere. This behavior suggests that many of the gravity waves may originate in the tropopause region and/or that waves are being reflected downward in the troposphere. Strelnikova et al. (2020) published Rayleigh lidar wind measurements made at ALOMAR, Norway ( $69.3^\circ\text{N}$ ,  $16.0^\circ\text{E}$ ) between 30 and 80 km in the stratosphere and mesosphere. They reported that 32.2% of all the detected gravity waves propagated downward. By analyzing the middle and upper atmosphere (MU) radar measurements at Shigaraki, Japan ( $34.9^\circ\text{N}$ ,  $139.4^\circ\text{E}$ ), Gavrilov et al. (1996) found that 44%–51% of the gravity waves in the altitude range of 70–80 km were propagating downward. Hu et al. (2002) employed a Na Doppler lidar to study gravity waves in the mesopause region between 84 and 104 km at SOR ( $35^\circ\text{N}$ ). Only 15.6% of all waves they observed were propagating downward, while 29% of the shorter vertical wavelength ( $\lambda_z < 11$  km) waves were propagating downward. A similar unpublished study was recently conducted with a Na Doppler lidar at Cerro Pachón, Chile ( $30^\circ\text{S}$ ) where 30.5% of the waves were observed to be propagating downward (Fabio Vargas, private communication, University of Illinois). Finally, numerical models of the southern hemisphere MLT developed by Becker and Vadas (2018), suggest that secondary wave generation is an important process in the mesosphere that can increase the fraction of downward propagating gravity wave energy. Furthermore, these secondary waves tend to have longer horizontal and vertical wavelengths than the primary waves from

which they are generated (Vadas et al., 2003, 2018). Therefore, the inferred  $\alpha_{\text{down}}$  profiles at McMurdo that are plotted in Figures 8a and 8b are in line with these previous studies and seem plausible.

### 6.3. Predicted Wave Mixing and Chemical Fluxes of Na

The measured Na flux is replotted in Figure 8c along with the wave mixing flux without Stokes drift given by the second term on the right-hand-side of Equation 17 and the wave mixing flux with Stokes drift given by first term on the right-hand-side of Equation 19. In both cases we used the  $K_{\text{wave}}$  profile plotted in Figure 7a that was derived according to Equation 20a. The Stokes drift velocity is plotted in Figure 6c. Clearly, the upward flux contribution from the Stokes drift at 84 km is important as it reduces the magnitude of the maximum downward Na flux so that the predicted Na flux profile caused by wave mixing is in much better agreement with the directly measured profile.

The metal layers are formed by meteoric ablation between about 80 and 115 km. Various dynamical processes transport the vaporized atoms and ions downward to chemical sinks below 90 km, where they form stable compounds, which then polymerize to form meteoric smoke particles (Plane et al., 2015). The chemical fluxes of the metal atoms are caused by wave-driven perturbations in their chemistry, which induces density fluctuations in the metals that are partially correlated with the vertical wind fluctuations of the waves. Between 80 and 100 km, the chemical loss rate of Na, due to its reaction with  $\text{O}_3$ , is significant. However, this reaction produces NaO, which then reacts with O, to quickly recycle the oxide back to Na. Because of this recycling, Na behaves much like an inert species above 90 km, where the meteoric influx is balanced by downward transport to maintain the steady state layer profile. Below 90 km, where the O density decreases rapidly with decreasing altitude, while the atmospheric density and the densities of  $\text{CO}_2$ ,  $\text{H}_2\text{O}$ , and  $\text{H}_2$  increase, this recycling of NaO is inhibited as Na is tied up in the more stable compound  $\text{NaHCO}_3$ . When  $\text{NaHCO}_3$  forms the dimer or polymerizes with other meteoric constituent molecules, Na is permanently removed from the gas phase (Plane et al., 2015). Above 95 km Na reacts with  $\text{O}_2^+$  and  $\text{NO}^+$  to form  $\text{Na}^+$  via charge transfer and during the day Na can be photoionized. However, during the long polar night in late May at McMurdo, neither of these charge transfer and photoionization processes play a significant role in Na chemistry.

The theoretical expression for the chemical flux of Na has been derived by Gardner and Liu (2016) and is given by

$$\overline{w' \rho_{\text{Na}}'}_{\text{Chemical}} \simeq \left[ \frac{(L_{\text{Na}} - \mu_{\text{Na}})}{\bar{\rho}_{\text{Na}}} \frac{\partial \bar{\rho}_{\text{Na}}}{\partial z} - \frac{\partial L_{\text{Na}}}{\partial z} \right] \frac{\text{Var}(T')}{(\Gamma_{\text{ad}} + \partial \bar{T} / \partial z)^2} \quad (22)$$

where  $\mu_{\text{Na}}$  is the meteoric injection rate profile for atomic Na and  $L_{\text{Na}}$  is the net chemical loss rate profile. Notice that the chemical flux, like  $E_{\text{pm}}$  and the wave mixing flux (which depends on  $K_E$ ), depends strongly on the normalized temperature variance plotted in Figure 3e. We compute  $L_{\text{Na}}$  by assuming that  $\text{NaHCO}_3$  is the primary reservoir for Na (Gardner et al., 2016; Gardner & Liu, 2016) and use  $\mu_{\text{Na}}$  derived from the CABMOD ablation model (Carrillo-Sánchez et al., 2020). The net Na loss is computed using the  $\text{H}_2$  profile predicted by WACCM, the  $\text{O}_3$ , O, H, and  $\text{H}_2\text{O}$  profiles measured by the SABER (Sounding of the Atmosphere using Broadband Emission Radiometry) instrument and the  $\text{CO}_2$  profile taken from ACE (Advanced Composition Explorer) as in Beagley et al. (2010). Unfortunately, SABER and ACE observations over McMurdo are only available in late April and late June so those measurements were averaged to estimate the late May profiles needed to compute  $L_{\text{Na}}$ .

To match the observed Na flux, all profiles of these minor species and two major species ( $\text{N}_2$  and  $\text{O}_2$ ) were shifted downward by  $\Delta z_{\text{down}} = 3.5$  km. We believe this is justified because the Na density (and Fe density, not shown) and flux profiles are displaced downward by about 3.5 km compared to lower latitudes, largely because of the strong downwelling over McMurdo at this time of year caused by the residual circulation system. Because not all the  $\text{NaHCO}_3$  is permanently lost and there are uncertainties in some of the reaction rates and species densities, we scaled the loss by 0.5 to obtain the best fit to the observed Na flux. This value is comparable to the 0.57 scaling used by Gardner et al. (2016) to match the Na chemical flux to the observations at SOR.

The chemical flux shown in Figure 8c is only significant on the bottomside of the Na layer where it is positive (upward) because  $\mu_{\text{Na}} < L_{\text{Na}}$  and  $\partial L_{\text{Na}} / \partial z < 0$ . The chemical flux of Na peaks near 79 km where it reaches  $\sim 2 \times 10^4 \text{ cm}^{-2} \text{ s}^{-1}$ . When the chemical flux profile is added to the wave mixing flux profile including Stokes drift (see Figure 8c, total theoretical Na wave flux curve), it reduces the negative wave mixing flux near and below 80 km, matching the observed



Na flux quite well in this region. Consequently, the total predicted Na flux profile given by Equations 17 and 19, is in better agreement with the directly measured Na flux profile at McMurdo than the Na wave mixing flux alone. These results demonstrate that the Stokes drift and chemical flux components make important, non-negligible contributions to the total vertical flux of mesospheric Na induced by non-breaking gravity waves.

#### 6.4. Eddy and Molecular Diffusion Fluxes

Although the McMurdo lidar data were processed in a way that did not include the additional vertical Na flux caused by eddy and molecular diffusion, their effects can be estimated by using the following formula (Gardner et al., 2019)

$$\overline{w'\rho_{\text{Na}}'}_{\text{Eddy+Mole}} = -\bar{\rho}_{\text{Na}} \left( \frac{g}{RT} + \frac{1}{T} \frac{\partial \bar{T}}{\partial z} + \frac{1}{\bar{\rho}_{\text{Na}}} \frac{\partial \bar{\rho}_{\text{Na}}}{\partial z} \right) \left[ 1 + \frac{\text{Var}(\partial T'/\partial z)}{(\Gamma_{\text{ad}} + \partial \bar{T}/\partial z)^2} \right] (K_{zz} + K_{\text{Mole}}). \quad (23)$$

$K_{zz}$  is the eddy diffusivity generated by breaking waves and  $K_{\text{Mole}}$  is the molecular diffusivity for Na. This expression is different from the classical formula because the diffusion is enhanced by the normalized lapse rate variance. This enhancement arises because the waves perturb the species mixing ratio gradients, which increases the mixing associated with turbulence and the thermal motion of the Na atoms (Gardner, 2018; Grygalashvyly et al., 2012). The instability parameter, expressed as the normalized lapse rate variance in Figure 3e, is mostly between 0.3 and 0.5 but reaches a maximum of 0.7 at 88 km where the environmental lapse rate approaches its largest positive value. Hence, the enhancement of eddy and molecular diffusion, while small, is non-negligible. The Na flux associated with eddy and molecular diffusion was computed by using the  $K_{zz}$  profile derived from WACCM simulations and the standard formula for the Na molecular diffusivity (Equation 35 in Gardner (2018)). Molecular diffusion of Na is only appreciable at the highest altitudes.

The estimated eddy and molecular diffusion fluxes were added to the measured Na flux associated with non-breaking waves and the resulting profile is plotted in Figure 8d. The Na transport velocities induced by molecular and eddy diffusion are compared with the measured wave-induced Na transport in Figure 6d. Although the eddy and molecular Na fluxes and transport velocities are non-negligible, they are much smaller than the wave contributions. This is not surprising because it has been known for decades that vertical transport induced by propagating gravity waves can be substantial. Walterscheid and Schubert (1989) used a dynamical-chemical model to show that the combined effects of wave dynamics and perturbed chemistry associated with the passage of a gravity wave can result in large downward fluxes of  $\text{O}_3$  and OH near 80 km, which alters the mixing ratios of these species and the eddy and molecular diffusion. Hickey et al. (2000) used a 2-D nonlinear model to demonstrate that gravity waves can significantly alter the time averaged atomic O profile in the MLT through the constituent fluxes that the waves induce. Their results showed clearly that the effects of gravity wave transport on the distribution of O in this region can be considerably larger than the effects of eddy transport. Liu and Gardner (2004, 2005) directly measured the vertical Na flux profiles induced by gravity waves in the MLT using a Na Doppler lidar coupled to large astronomical telescopes at SOR (35°N) and Haleakala, Maui (20°N). Those observations also showed that wave transport of Na was generally much larger than transport by eddy and molecular diffusion.

Despite this early work and the significant heat and Na fluxes reported here, few, if any, of the global atmospheric chemical models incorporate heat and constituent transport by non-breaking gravity waves, because they cannot resolve the important smaller-scale waves. However, this situation is now changing. Grygalashvyly et al. (2012) employed an effective wave diffusivity, equivalent to the enhanced eddy and molecular diffusivities given by Equation 23, and a numerical model to study the impact of gravity waves on the transport of minor constituents in the MLT. Gardner and Liu (2016) derived generalized theoretical expressions for the chemical fluxes of neutral species induced by waves and turbulence and explored the impact on the transport of  $\text{O}_3$ , Na, and Fe in the MLT. Gardner et al. (2019) showed how the Stokes drift, chemical fluxes,  $K_{\text{Wave}}$ , and the enhanced eddy and molecular diffusivities can be derived from most gravity wave parameterizations incorporated in global models. Most recently, Liu (2021) employed the concept of scale invariance to extrapolate the thermal diffusivity ( $K_H$ ) arising

from the large-scale waves resolved by global models, to include the contributions to  $K_H$  from the unresolved small-scale waves. This approach could be adapted to also calculate  $K_{Wave}$ .

## 7. Discussion

### 7.1. Impact of the Complete Temporal Spectrum of Gravity Waves

An important characteristic of the McMurdo observations is that the flux measurements represent the contributions from the entire temporal spectrum of gravity waves, while all the previous measurements excluded waves with periods longer than the mean observation periods ( $\sim 6$ – $10$  hr). Guo and Liu (2021) showed that the major contributions to the sensible heat and potential temperature fluxes were made by waves with periods between 5 min and 1 hr. The contributions from longer period waves (1–3 and 3–6 hr) were small by comparison. The heat flux measurements at the Starfire Optical Range, Cerro Pachón, and McMurdo are comparable ( $\sim 2.5$  Kms/s, see Table 1) and all were made with temporal resolutions sufficient to observe the highest frequency waves with periods as short as the buoyancy period. The heat flux measurements at Hefei were made with a temporal resolution of 10 min, which excludes the highest frequency waves with periods smaller than 20 min and could partially account for the very low heat flux value ( $-0.3$  Kms $^{-1}$ ) at this site. The Maui observations also included the highest frequency waves so the lower heat flux value there ( $-1.4$  Kms $^{-1}$ ), probably reflects both weaker gravity wave activity at this mid-ocean site and the fact that the Maui value represents the annual mean, not late fall when wave activity should be stronger.

Although the Na flux depends in part on the sensible heat flux through  $K_{Wave}$  as given by Equation 18,  $K_{Wave}$  also has a strong dependence on the total temperature variance through  $K_E$  as given by Equation 12. Because the temperature fluctuations have a red frequency spectrum, roughly proportional to  $\omega^{-2}$ , the longest period waves make the largest contributions to  $K_E$  and  $K_{Wave}$  and therefore to the Na flux. Only the McMurdo flux observations include contributions from the complete temporal spectrum of gravity waves and in particular, the observations include the persistent inertial-period gravity waves (Chen & Chu, 2017; Chen et al., 2016) that are missing from the other sites. This is important for the constituent fluxes. For example, if we scale the SOR Na flux value in late Nov by the ratio of the Na densities ( $\sim 5,000/6,500$ ) times the  $3/2$  power of the ratio of the  $T'$  variances ( $\sim (110/60)^{3/2}$ , to account for the larger values of  $K_E$  and  $K_{Wave}$  at McMurdo), we obtain  $-4.3 \times 10^4$  cm $^{-2}$ s $^{-1}$ , which is comparable to the McMurdo Na flux measurement in late May. Thus, the large McMurdo Na flux appears reasonable and illustrates the important contributions that inertial-period gravity waves make to atmospheric mixing and constituent transport in the MLT.

### 7.2. Impact of Downward-Propagating Gravity Waves

To match the theoretical Na fluxes with the lidar observations between 89 and 95 km, we inferred that a majority ( $>50\%$ ) of the wave energy was associated with downward-propagating gravity waves. Wave ducting and reflections from above can contribute to downward propagating waves, as well as in-situ wave generation. The similarity of the lidar-observed  $E_{pm}$  profile (Figure 4a) to the modeled profile shown in Figure 20 of Vadas and Becker (2019), suggests that the generation of secondary (and tertiary) gravity waves by the body forces produced from the dissipation of primary (and secondary) waves is likely to be a major source of downward propagating waves, especially in the region of 89–95 km where dissipation is significant (Becker & Vadas, 2018; Vadas et al., 2018; Vadas & Becker, 2018, 2019). Moreover, Joule heating and energetic particle precipitation over McMurdo likely provide extra sources of gravity waves in the lower thermosphere, which would also contribute to the downward-propagating gravity waves at lower altitudes.

### 7.3. Possible Heat Sources and Wave Amplification in the Lower Thermosphere

McMurdo is located by the edge of auroral oval and polar cap, where energy input from the magnetosphere frequently reaches the bottom of the thermosphere via particle precipitation and Joule heating (e.g., Sinnhuber et al., 2012; Thayer & Semeter, 2004) and the Farley-Buneman instability can also contribute to the heating of the neutral atmosphere (e.g., Dimant & Oppenheim, 2011a, 2011b). Various forms of energy, such as mechanical, chemical, and electrical-magnetic energy as well as solar radiation energy (during daytime), can be converted to the thermal energy of the neutral atmosphere (e.g., Mlynczak & Solomon, 1993; Sinnhuber et al., 2012).

Therefore, external heat sources are possible in the lower thermosphere at McMurdo, originating from energy input and forcing from the magnetosphere and ion-neutral coupling, such as Joule heating and energetic particle precipitation, as well as from solar radiation and chemical heating. Indeed, intense aurora emissions at a wavelength of 557.7 nm were observed overhead at McMurdo as well as in the auroral zone during the lidar observation periods with a collocated auroral all-sky camera that was developed by the National Institute of Polar Research (NIPR), Japan and installed at Arrival Heights (Ogawa et al., 2020). An example image of the aurora observations at Arrival Heights on 26 May 2020 is shown in the Supporting Information S1 (Figure S3). The aurora observations provide evidence that heating occurred in the lower thermosphere because the altitude of green-line aurora emissions is usually around 100–120 km (e.g., Kurihara et al., 2009). Although McMurdo was in the darkness during the lidar observations, solar energy could be stored and then transported to McMurdo from other sunlit areas and released as chemical heating (Mlynczak & Solomon, 1993).

Moreover, lidar observations at McMurdo have demonstrated the super-exponential amplitude growth for tides and planetary waves in the altitude range from 100 to 110 km (Fong et al., 2014, 2015; Lu, Chu, Chen, et al., 2017). Fong et al. (2014, 2015) reported that the super-exponential growth increases in strength with the  $K_p$  magnetic activity index. The tidal results were attributed to a magnetospheric source origin, that is, in situ generated mainly by polar ionospheric convection and Joule heating (Fong et al., 2015). Lu, Chu, Chen, et al. (2017) report that the amplitudes of 4-day and 2.5-day planetary waves in temperatures also grow rapidly from 1 to 2 K at 100 km to over 10 K at 110 km in May 2014. A seeding-amplification scheme was proposed in Lu, Chu, Chen, et al. (2017) as the mechanism to amplify surviving 4-day and 2.5-day planetary waves by in situ instabilities. The positive (upward) sensible heat flux reported here aligns well with these earlier findings in the lower thermosphere at McMurdo.

Wave dissipation converting wave mechanical (kinetic and potential) energy to thermal energy can naturally proceed with 100% conversion rate; however, the opposite direction of the process does not happen easily because of the increase of entropy principle. Nevertheless, wave amplification converting thermal or other energy into wave mechanical energy can happen, although it will likely be inefficient and will need some mechanisms (e.g., nonlinearities) to achieve. A possible scenario could be that localized heating forms pressure differences so generate large wind shears, leading to instabilities and/or nonlinearities. We speculate that the instabilities/nonlinearities caused by large wind shears could induce wave amplification and/or cause negative phase shift between  $w'$  and  $T'$ , that is,  $\Delta\phi_{w'T'} < 0$ , which would lead to positive sensible heat and potential temperature fluxes. The mechanisms of wave amplification and their impact on sensible heat and potential temperature fluxes are beyond the scope of this study but these issues deserve further attention, both theoretically and observationally.

#### 7.4. Wave-Driven Heating/Cooling Rate and Na Production/Loss Rate

Examination of the  $\bar{T}$  profile reveals that there is a small inversion layer near 85 km with a full width of about 5 km where the temperature is 5–10 K warmer than the nominal upper mesospheric profile. This inversion layer may result from local heating caused by gravity waves dissipating in this region, as well as to the transport of heat downward from above. The heating rate due to heat flux convergence is

$$-\frac{1}{\bar{\rho}_A} \frac{\partial (\bar{\rho}_A \overline{w'T'})}{\partial z} = -\frac{\partial \overline{w'T'}}{\partial z} + \left( \frac{g}{RT} + \frac{1}{T} \frac{\partial \bar{T}}{\partial z} \right) \overline{w'T'}. \quad (24)$$

The heating rate profile is plotted in Figure 9a. Also plotted in Figure 9a is the heating/cooling rate associated with eddy heat transport, which is clearly much smaller compared to the significant impact of transport caused by non-breaking waves. The heating rate induced by non-breaking waves approaches nearly  $65 \text{ Kd}^{-1}$  at 82.5 km while the cooling rate is about  $-75 \text{ Kd}^{-1}$  at 85 km. The temperature variance reaches a local maximum of  $110 \text{ K}^2$  at 85 km (Figure 3a). In addition, because  $K_{\text{Wave}}$  is large near 85 km (Figures 7c and 7f), the fast downward transport of O into this region will contribute to increased chemical heating associated with the exothermic reactions involving the excess O. Because the inversion layer is small, the large heating caused by breaking waves, wave-induced heat transport, and odd-O reactions, must be balanced by cooling, which could result from wave-transport of  $\text{CO}_2$  upward from below. The  $\text{CO}_2$  mixing ratio is relatively constant in the lower mesosphere but exhibits a knee in the profile near 78 km and falls off above (Beagley et al., 2010). Thus, the enhanced wave mixing characterized by large  $K_{\text{Wave}}$  values above 80 km, would increase the upward transport  $\text{CO}_2$  into

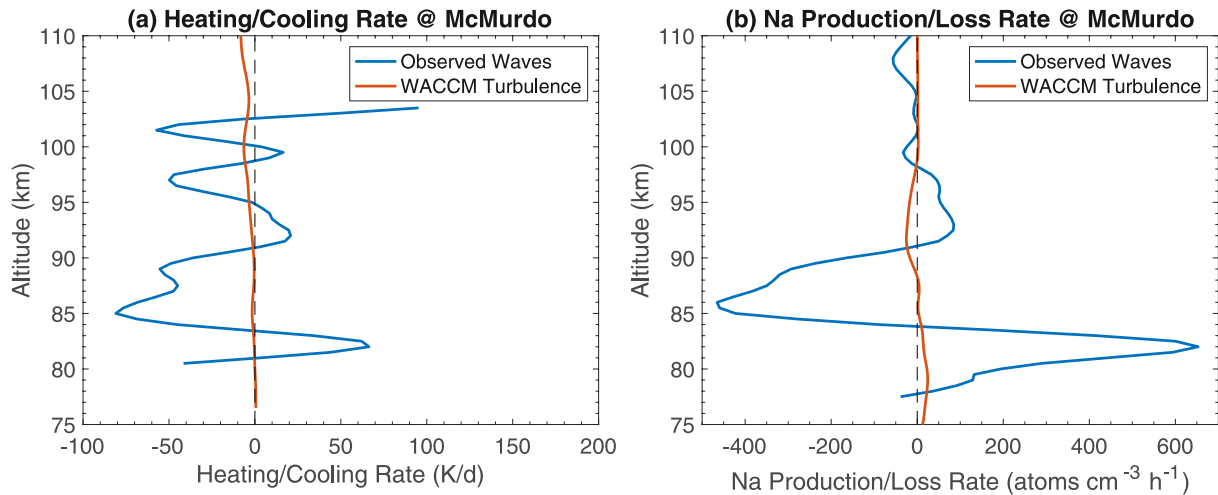


**Figure 9.** (a) Profiles of the heating/cooling rates associated with the convergence of wave-mixing heat flux and eddy heat flux. (b) Corresponding profiles of the Na production/loss rates associated with the convergence of Na wave-mixing flux and eddy flux.

this region, which in turn would increase the radiative cooling via  $\text{CO}_2$  infrared emissions. Of course, the large values of  $K_{\text{Wave}}$  are due in part to the relatively large negative vertical gradient of temperature (i.e., positive environmental lapse rate) associated with the inversion layer which also affects the values of  $K_H$  and  $K_E$  as seen in Equations 9–11. However, as seen in Figure 7a,  $K_{\text{Wave}}$  is negative above 90 km, which would inhibit the downward transport of O in this region, thereby reducing the impact of chemical heating needed to balance the large cooling rate observed at 97 and 102 km. We acknowledge that this discussion of the influence of gravity waves on the measured temperature structure at McMurdo is speculative and difficult to reconcile with the observed heating rate profile. Unfortunately, until models fully incorporate the constituent and heat transport processes induced by unresolved gravity waves, it will not be possible to obtain a clear understanding of the precise roles that wave-driven transport plays in the thermal balance of the MLT.

The low 84 km peak in the Na flux is probably caused primarily by the strong downwelling over the polar cap in May, but enhanced downward wave transport of Na may also play a role. The measured McMurdo Na layer is highly asymmetric with a peak near 88 km, which is several km lower than observed at mid-latitudes or even at the South Pole at this time of year. The direct effect of vertical constituent transport is local production or loss of the constituent. The production/loss rate of Na due to vertical flux convergence is

$$P_{\text{Na}} = -\frac{\partial w' \rho'_{\text{Na}}}{\partial z}. \quad (25)$$

The Na production/loss rate profile induced by non-breaking waves is plotted in Figure 9b. The Na production rate is about  $620 \text{ Na atoms cm}^{-3} \text{ hr}^{-1}$  at 82 km. This is balanced by increased chemical loss, which is proportional to  $\rho_{\text{Na}}$ , to maintain the steady-state layer profile. Above 84 km the production rate is negative, reflecting a loss rate that peaks at about  $-420 \text{ Na atoms cm}^{-3} \text{ hr}^{-1}$  at 86 km. This loss results in a reduction of the Na density in this region because the meteoric influx ( $\sim 10\text{--}20 \text{ cm}^{-3} \text{ hr}^{-1}$ ) does not change. Therefore, the transport loss of Na between 84 and 90 km, in combination with the strong wintertime downwelling, helps lower the peak of the Na profile to 88 km. For comparison the Na production/loss rate associated with eddy transport by turbulence is also plotted in Figure 9b. As expected, the impact of eddy transport is small compared to the significant impact of Na transport by non-breaking waves.

## 8. Conclusions

The high southern latitude of McMurdo allows continuous long-duration lidar observations in late May, enabling the coverage of the complete temporal spectrum of gravity waves from the buoyancy period ( $\sim 5 \text{ min}$ ) to the inertial period ( $\sim 12.3 \text{ hr}$ ). These Na Doppler lidar observations, made with high signal-to-noise ratios, coupled with the interleaved data processing technique, allow the extension of vertical flux and transport measurements



upward to  $\sim 110$  km and downward to  $\sim 78$  km, basically doubling the altitude range of 85–100 km studied at mid- and low-latitudes. Located by the edge of auroral oval and polar cap where the downwelling associated with the residual general circulation is strong, the McMurdo lidar observations have led to several surprising discoveries.

First, the downward Na flux peak is located at 84 km, which is about 4 km lower than observed at midlatitudes, and the magnitude is double the maximum at midlatitudes. The lower peak altitude is likely related to the strong downwelling and wave-driven transport over McMurdo in late May, while the large downward flux is probably related to the enhanced downward wave transport by the energetic inertial-period gravity waves frequently observed at McMurdo. This study represents the first-ever flux measurements that include the contributions from such persistent inertial-period waves and from the complete temporal spectrum of gravity waves.

Second, to achieve good agreement between the predicted and measured Na flux, we inferred that in the region between 89 and 95 km, where wave dissipation was significant, a majority ( $>50\%$ ) of the gravity wave energy was propagating downward. The lidar-observed profiles of temperature variance and gravity wave potential energy density exhibit two local maxima around 85 and 112 km, which are quite similar in shape to the  $E_{\text{pm}}$  profile modeled by Vadas and Becker (2019) for secondary and tertiary wave generation. We hypothesize that the large fraction of downward propagating wave energy may be associated with secondary (and tertiary) waves generated by the dissipation of primary (and secondary) waves, which lends support to the multistep vertical coupling proposed by Vadas and Becker (2018, 2019).

Third, the measured sensible heat flux exhibits a downward peak at 84 km that is comparable to the peak values at midlatitudes but lower by about 4 km, while the sensible heat flux is directed upward (positive) in the lower thermosphere from 97 to 106.5 km. Although we have focused in this paper on the late May 2020 observations, measurements made on numerous other occasions show that positive heat fluxes are common in the lower thermosphere in winter above McMurdo. We have shown that the positive sensible heat flux is actually expected from the fully compressible polarization relations for non-dissipative gravity waves. Although the large positive heat fluxes observed above 100 km could be induced by a suitable spectrum of upward-propagating, non-dissipating gravity waves, the observed heat and Na fluxes in this region suggest that other factors, such as external heat sources and wave amplification, may also play important roles, possibly through affecting the phase shift between  $w'$  and  $T'$ .

The McMurdo lidar observations illustrate the substantial impact that wave-induced transport can have on the temperature and constituent structures of the MLT. These measurements show that transport associated with Stokes drift imparted by the gravity wave spectrum, chemical transport of reactive species like Na and other meteoric metals, and wave transport associated with atmospheric mixing by non-breaking gravity waves, can all make significant contributions to constituent and heat transport in the MLT. While this study focused on heat and Na transport, wave transport also impacts other important MLT species including  $\text{O}_x$ ,  $\text{NO}_x$ ,  $\text{HO}_x$ ,  $\text{CO}_2$  and potentially neutral density and the  $\text{O}/\text{N}_2$  ratio in the thermosphere, which impacts satellite drag. It is now clear that these mechanisms should be incorporated in the next generation of global chemistry and general circulation models to fully understand how gravity waves influence the structure and composition of the middle and upper atmosphere. Furthermore, advanced transport theories and fully compressible polarization relations of gravity waves, which account for heat sources and sinks, and for wave dissipation and amplification, should be developed in the future.

## Appendix A: Derivation of the Effective Diffusivity Associated With the Energy Flux

As shown by Liu (2009) and extended by Gardner (2018), the gravity wave polarization relations can be used to express the gravity wave energy flux and  $K_E$  in terms of the temperature fluctuation spectrum as follows

$$K_E = \kappa \frac{g}{N^2} \frac{\overline{w'p'}}{\bar{p}} \simeq \frac{\kappa (1 - 2\alpha_{\text{down}})}{H_p (\Gamma_{\text{ad}} + \partial \bar{T} / \partial z)^2} \frac{1}{(2\pi)^2} \int d\omega \int dm \left(1 - \frac{\omega^2}{N^2}\right) \frac{\omega}{m} \frac{m^2 F_{T'}(m, \omega)}{[m^2 + (1 - 2\kappa\omega^2/N^2)/(2H_p)^2]}, \quad (\text{A1})$$

where  $\alpha_{\text{down}}$  is the fraction of wave energy propagating downward,  $F_{T'}(m, \omega)$  is the 2-D power spectrum of the wave-induced temperature fluctuations,  $\omega$  is the intrinsic frequency, and  $m$  is the vertical wavenumber. The right-hand-side of Equation A1 was derived by assuming that the shapes, but not the absolute magnitudes, of the spectra for the upward and downward propagating waves are identical, hence the approximately equal sign is used.

To evaluate Equation A1 we employ the diffusive filtering theory model spectrum, also used by Gardner (2018), so that

$$F_{T'}(m, \omega) = (2\pi)^2 \frac{\text{Var}(T')}{[1 - (f/N)^{q-1}]} \frac{(s+1)}{m_*} \left(\frac{m}{m_*}\right)^s \frac{(q-1)}{f} \left(\frac{f}{\omega}\right)^{q+(s+1)/2} m \leq m_* \sqrt{\omega/f}, f \leq \omega \leq N \quad (\text{A2})$$

where  $m_*$  is the characteristic vertical wavenumber. Under these conditions the 1-D  $\omega$ -spectrum is proportional to  $1/\omega^q$  and the 1-D  $m$ -spectrum is proportional  $1/m^{2q-1}$  in the region  $m_* \leq m$ . The largest wavenumber  $m_* \sqrt{N/f}$  marks the transition from waves to turbulence.

Extensive observations, made at a wide variety of locations and altitudes by many different instruments have shown, that the  $\omega$ - and  $m$ -spectra of the horizontal wind and temperature fluctuations follow power-laws of the form  $\omega^{-r}$ , where  $r \approx 2$ , and  $m^{-t}$  in the region  $m_* < m$ , where  $t \approx 3$ . The model spectrum given by Equation A2 is consistent with this observed behavior for the special case where  $q \approx 2$ . Furthermore, several theories predict that the  $m$ -spectrum magnitude remains approximately constant with altitude in the so-called saturation regime  $m_* < m$ , so that as the wave field propagates upward,  $m_*$  decreases to accommodate the increasing variance of  $T'$ . The characteristic vertical wavenumber can be expressed in terms of the variance of the lapse rate fluctuations

$$\begin{aligned} \text{Var}(\partial T'/\partial z) &= m_*^2 \frac{1}{(2\pi)^2} \int d\omega \int dm \left(\frac{m}{m_*}\right)^2 F_{T'}(m, \omega) \\ &= m_*^2 \frac{\text{Var}(T')}{[1 - (f/N)^{q-1}]} \frac{(s+1)}{(s+3)} \begin{cases} \ln(N/f) \text{ for } q = 2 \\ \frac{(q-1)}{(2-q)} [(N/f)^{2-q} - 1] \text{ for } q \neq 2 \end{cases} \end{aligned} \quad (\text{A3})$$

which yields

$$\frac{1}{m_*^2} = \frac{\text{Var}(T')}{\text{Var}(\partial T'/\partial z)} \frac{(s+1)}{(s+3)} \frac{1}{[1 - (f/N)^{q-1}]} \begin{cases} \ln(N/f) \text{ for } q = 2 \\ \frac{(q-1)}{(2-q)} [(N/f)^{2-q} - 1] \text{ for } q \neq 2 \end{cases} \quad (\text{A4})$$

$K_E$  can now be computed by substituting Equation A2 into A1, neglecting the small contributions from terms involving  $(\omega/N)^2$ , and noting that  $1 \ll 2H_p m_*$

$$\begin{aligned} K_E &\simeq \frac{\kappa(1 - 2\alpha_{\text{down}})}{H_p (\Gamma_{\text{ad}} + \partial \bar{T}/\partial z)^2} \frac{f}{m_*} \frac{1}{(2\pi)^2} \int d\omega \int dm \frac{\omega}{f} \frac{m_*}{m} F_{T'}(m, \omega) \simeq \\ &(1 - 2\alpha_{\text{down}}) \frac{\Gamma_{\text{ad}} f}{\bar{T} m_*} \frac{\text{Var}(T')}{(\Gamma_{\text{ad}} + \partial \bar{T}/\partial z)^2} \frac{(s+1)(q-1)}{s [1 - (f/N)^{q-1}]} \begin{cases} \frac{1 - (f/N)^{q-3/2}}{(q-3/2)} \text{ for } q \neq 3/2 \\ \ln(N/f) \text{ for } q = 3/2 \end{cases}. \end{aligned} \quad (\text{A5})$$

By applying Equation A4,  $K_E$  reduces to

$$K_E \simeq (1 - 2\alpha_{\text{down}}) \beta(s, q) \frac{\Gamma_{\text{ad}} f}{\bar{T} \sqrt{\xi_{\text{inst}}}} \left[ \frac{\text{Var}(T')}{(\Gamma_{\text{ad}} + \partial \bar{T}/\partial z)^2 [1 - (f/N)^{q-1}]} \right]^{3/2}, \quad (\text{A6})$$

where  $[1 - (f/N)^{q-1}] \simeq 1$  for  $3/2 \leq q$  and

$$\beta(s, q) = \begin{cases} \frac{2(s+1)}{s} \sqrt{\frac{(s+1)\ln(N/f)}{(s+3)}} (1 - \sqrt{f/N}) \text{ for } q = 2 \\ \frac{(s+1)}{2s} \sqrt{\frac{(s+1)(\sqrt{N/f} - 1)}{(s+3)}} \ln(N/f) \text{ for } q = 3/2, \\ \frac{(s+1)(q-1)}{s(q-3/2)} \sqrt{\frac{(s+1)(q-1) [(N/f)^{2-q} - 1]}{(s+3)(2-q)}} [1 - (f/N)^{q-3/2}] \text{ for } q \neq 2 \text{ or } 3/2 \end{cases} \quad (\text{A7})$$

**Table A1**  
 $\beta(s, q)$  for  $N/f = 148$  at McMurdo

$s$	$q$	$\beta(s, q)$
1	2	5.801
1/2	2	8.056
1	5/3	9.356
1/2	5/3	12.99
1	3/2	11.79
1/2	3/2	16.38

and  $\xi_{\text{inst}}$  is the normalized lapse rate variance  $(\text{Var}(\partial T'/\partial z)/(\Gamma_{\text{ad}} + \partial \bar{T}/\partial z))^2$

which is also called the instability parameter. The normalized lapse rate variance can be expressed in terms of Richardson number by expressing the temperature fluctuations in terms of the horizontal wind fluctuations by employing the gravity wave polarization relations

$$T' \simeq \frac{N\bar{T}}{g} u'. \quad (\text{A8})$$

After neglecting terms  $\partial \bar{T}/\partial z$  and  $\partial N/\partial z$ , we obtain

$$\xi_{\text{inst}} = \frac{\text{Var}(\partial T'/\partial z)}{(\Gamma_{\text{ad}} + \partial \bar{T}/\partial z)^2} \simeq \frac{\text{Var}(\partial u'/\partial z)}{N^2} = 1/Ri. \quad (\text{A9})$$

$\beta(s, q)$  is tabulated in Table A1 for several values of  $s$  and  $q$  for McMurdo where the inertial period is 12.3 hr and the buoyance period is approximately 5 min.

## Appendix B: Uncertainties of the Estimated Sample Variances and Fluxes

The uncertainties of the estimated sample variances and fluxes were derived following the approaches described in the appendices of Gardner and Yang (1998) and Gardner and Chu (2020). By considering the vertical smoothing associated with the Hamming window, the uncertainty associated with estimating the fluctuation variance of the physical variable  $X$  from the sample covariance function is

$$\Delta \text{Var}(X') \simeq \sqrt{2 \frac{L_{X'}}{L_{\text{sm}}} \frac{\tau_{X'}}{\tau_{\text{obs}}} \text{Var}^2(X') + \frac{\Delta z}{L_{\text{sm}}} \frac{\Delta t}{\tau_{\text{obs}}} [2 \text{Var}(X') \text{Var}(\Delta X) + \text{Var}^2(\Delta X)]}. \quad (\text{B1})$$

where prime represents the fluctuations of  $X$  and  $X' = T'$ ,  $\partial T'/\partial z$ ,  $w'$ ,  $\rho'_{\text{Na}}$ .  $L_{\text{sm}} \simeq 3.42$  km is the equivalent rectangular window width of the 5 km full-width Hamming window and  $\tau_{\text{obs}} = 40$  hr is total observation time. Because the vertical correlation lengths of  $T'$ ,  $\frac{\partial T'}{\partial z}$ , and  $\rho'_{\text{Na}}$  are long compared to the smoothing interval, for these parameters  $L_{X'} = L_{\text{sm}}$  and so smoothing does not reduce the uncertainty associated with statistical noise. However, vertical smoothing does reduce the uncertainty associated with photon noise which is important at the lowest and highest altitudes where the Na densities and signal levels are small. For the vertical wind fluctuations, which exhibit a nearly white m-spectrum (Gardner & Yang, 1998),  $L_{w'} \simeq \Delta z$ . The  $T'$  spectra published by Chen et al. (2016) for the wintertime MLT above McMurdo show that the  $\omega$ -spectra are significantly enhanced near  $\omega \simeq 2f$  by the presence of persistent waves with periods between  $\sim 3$  and  $\sim 10$  hr. This enhancement also distorts the spectral slopes at higher frequencies making them steeper. We considered the impact of these persistent waves by modeling the  $T'$   $\omega$ -spectrum as proportional to  $\omega$  for  $f \leq \omega \leq 2f$  and proportional to  $\omega^{-2}$  for  $2f \leq \omega \leq N$ . For this model, we computed  $\tau_{T'} = \tau_{\text{Na}} \simeq 1$  hr. Although the persistent waves will also impact the lapse rate spectra, the effects are minor and so we used the correlation time (15 min) derived in Gardner and Chu (2020). The vertical wind  $\omega$ -spectrum is approximately white so that  $\tau_{w'} \simeq 2.5$  min.

The uncertainty associated with estimating the vertical flux of the physical variable  $X$  from the sample covariance between the vertical wind and the physical variable ( $T'$  or  $\rho'_{\text{Na}}$ ) fluctuations is

$$\Delta \left( \overline{w'X'} \right) \simeq \sqrt{\frac{L_{w'X'}}{L_{\text{sm}}} \frac{\tau_{w'X'}}{\tau_{\text{obs}}} \text{Var}(w') \text{Var}(X') + \frac{\Delta z}{2L_{\text{sm}}} \frac{\Delta t}{\tau_{\text{obs}}} [\text{Var}(w') \text{Var}(\Delta X) + \text{Var}(\Delta w) \text{Var}(X') + \text{Var}(\Delta w) \text{Var}(\Delta X)]}. \quad (\text{B2})$$

The vertical correlation length and correlation times for fluxes are determined by the vertical wind so that  $L_{w'X'} \simeq \Delta z$  and  $\tau_{w'X'} \simeq \Delta t$ . The factor of 1/2 in Equation B2 arises because we derived two estimates of the vertical fluxes from the two interleaved  $w'$  and  $X'$  time series and averaged them. The photon noise components contaminating the two flux estimates are statistically independent, while the statistical noise components are identical.

The above uncertainties, derived under the assumption of stationary ergodic random processes, include contributions from the statistical noise associated with the calculation of the sample covariances and fluxes (i.e., the  $\text{Var}^2(X')$  and  $\text{Var}(w')\text{Var}(X')$  terms) and from the photon noise associated with the Poisson distribution of photon counting (i.e., the  $\text{Var}^2(\Delta X)$  and  $\text{Var}(\Delta X)$  terms). The equations used to estimate the rms uncertainties for the measured variances and fluxes in this study are listed in Table B1.

**Table B1**

*RMS Uncertainties of the Estimated Variances and Fluxes for McMurdo Observations<sup>a</sup>*

Wave-Driven Temperature Variance:  $\tau_T \approx 1$  hr,  $\Delta t = 2.5$  min,  $\tau_{\text{obs}} \approx 40$  hr,  $L_T \approx L_{\text{sm}} \approx 3.42$  km

$$\Delta \text{Var}(T') \approx \sqrt{\frac{1}{20} \text{Var}^2(T') + \frac{0.28}{960} [2\text{Var}(T') \text{Var}(\Delta T) + \text{Var}^2(\Delta T)]}$$

Wave-Driven Lapse Rate Variance:  $\tau_{\partial T/\partial z} \approx 15$  min,  $\Delta t = 2.5$  min,  $\tau_{\text{obs}} \approx 40$  hr,  $L_{\partial T/\partial z} \approx L_{\text{sm}} \approx 3.42$  km

$$\Delta \text{Var}(\partial T'/\partial z) \approx \sqrt{\frac{1}{80} \text{Var}^2(\partial T'/\partial z) + \frac{0.28}{960} [2\text{Var}(\partial T'/\partial z) \text{Var}(\partial \Delta T/\partial z) + \text{Var}^2(\partial \Delta T/\partial z)]}$$

Wave-Driven Vertical Wind Variance:  $\tau_{w'} \approx 2.5$  min,  $\Delta t = 2.5$  min,  $\tau_{\text{obs}} \approx 40$  hr,  $L_{w'} \approx \Delta z = 0.96$  km,  $L_{\text{sm}} \approx 3.42$  km

$$\Delta \text{Var}(w') \approx \sqrt{\frac{0.28}{480} \text{Var}^2(w') + \frac{0.28}{960} [2\text{Var}(w') \text{Var}(\Delta w) + \text{Var}^2(\Delta w)]}$$

Wave-Driven Na Density Variance:  $\tau_{\rho'_{\text{Na}}} \approx 1$  hr,  $\Delta t = 2.5$  min,  $\tau_{\text{obs}} \approx 40$  hr,  $L_{\rho'_{\text{Na}}} \approx L_{\text{sm}} \approx 3.42$  km

$$\Delta \text{Var}(\rho'_{\text{Na}}) \approx \sqrt{\frac{1}{20} \text{Var}^2(\rho'_{\text{Na}}) + \frac{0.28}{960} [2\text{Var}(\rho'_{\text{Na}}) \text{Var}(\Delta \rho_{\text{Na}}) + \text{Var}^2(\Delta \rho_{\text{Na}})]}$$

Wave-Driven Sensible Heat Flux:  $\tau_{w'T'} \approx 2.5$  min,  $\Delta t = 2.5$  min,  $\tau_{\text{obs}} \approx 40$  hr,  $L_{w'T'} \approx \Delta z = 0.96$  km,  $L_{\text{sm}} \approx 3.42$  km

$$\Delta \left( \overline{w'T'} \right) \approx \sqrt{\frac{0.28}{960} \text{Var}(w') \text{Var}(T') + \frac{0.28}{1920} [\text{Var}(w') \text{Var}(\Delta T) + \text{Var}(\Delta w) \text{Var}(T') + \text{Var}(\Delta w) \text{Var}(\Delta T)]}$$

Wave-Driven Na Flux:  $\tau_{w'\rho'_{\text{Na}}} \approx 2.5$  min,  $\Delta t = 2.5$  min,  $\tau_{\text{obs}} \approx 40$  hr,  $L_{w'\rho'_{\text{Na}}} \approx \Delta z = 0.96$  km,  $L_{\text{sm}} \approx 3.42$  km

$$\Delta \left( \overline{w'\rho'_{\text{Na}}} \right) \approx \sqrt{\frac{0.28}{960} \text{Var}(w') \text{Var}(\rho'_{\text{Na}}) + \frac{0.28}{1920} [\text{Var}(w') \text{Var}(\Delta \rho_{\text{Na}}) + \text{Var}(\Delta w) \text{Var}(\rho'_{\text{Na}}) + \text{Var}(\Delta w) \text{Var}(\Delta \rho_{\text{Na}})]}$$

<sup>a</sup> $\text{Var}(X')$  is obtained from the interleaved method while  $\text{Var}(\Delta X)$  is 2 times the difference between the total and wave-driven variances (Gardner & Chu, 2020).

## Appendix C: Heat and Energy Fluxes for Compressible Gravity Waves

To characterize the sensible heat flux contributed by an individual wave, we employ an idealized model for the vertical wind and temperature fluctuations induced by a wave of ground-based frequency  $\omega_r$ , intrinsic frequency  $\omega$ , and vertical wavenumber  $m$

$$w'(t) = A_w \cos(\omega_r t - mz - \phi_w) \quad (\text{C1})$$

$$T'(t) = A_T \cos(\omega_r t - mz - \phi_T) \quad (\text{C2})$$

where  $A_w$  and  $A_T$  are the wave amplitudes,  $\phi_w$  and  $\phi_T$  are the phases for the maximum fluctuations, and  $t$  and  $z$  are time and altitude, respectively. The sensible heat flux induced by the wave is calculated by averaging the product  $w'(t)T'(t)$  over the wave period (denoted by the overbar),

$$\overline{w'(t)T'(t)} = \frac{1}{2} A_w A_T \cos(\phi_w - \phi_T). \quad (\text{C3})$$

The compressible, f-plane, non-dissipative polarization relation for  $w'(t)$  and  $T'(t)$  is given by Equation B11 in Vadas (2013), which can be written as

$$w' = \frac{-ig\omega}{N^2} \frac{\left[1 - \frac{i}{mH} \left(\frac{1}{2} - \frac{1}{\gamma}\right)\right]}{\left[1 + \frac{i}{mH} \left(\frac{1}{2} - \frac{\gamma-1}{\gamma} \frac{\omega^2}{N^2}\right)\right]} \frac{T'}{T} = \frac{g\omega}{N^2} \frac{\left[1 + \frac{1}{(mH)^2} \left(\frac{1}{2} - \frac{1}{\gamma}\right)^2\right]^{1/2}}{\left[1 + \frac{1}{(mH)^2} \left(\frac{1}{2} - \frac{\gamma-1}{\gamma} \frac{\omega^2}{N^2}\right)^2\right]^{1/2}} e^{-i(\phi_w - \phi_T)} \frac{T'}{T}, \quad (\text{C4})$$

where  $m$  is negative for upward propagating waves,  $\gamma = C_p/C_v \approx 1.4$  for  $z \sim 100$  km, and the phase difference between  $w'(t)$  and  $T'(t)$  is

$$\phi_w - \phi_T = \frac{\pi}{2} + \tan^{-1} \left[ \frac{1}{mH} \left( \frac{1}{2} - \frac{1}{\gamma} \right) \right] + \tan^{-1} \left[ \frac{1}{mH} \left( \frac{1}{2} - \frac{\gamma-1}{\gamma} \frac{\omega^2}{N^2} \right) \right]. \quad (C5)$$

Note that in applying the Vadas (2013) polarization relations, we make the reasonable assumption that the hatted quantities at a fixed altitude may be replaced by primed quantities. The sensible heat flux for this single wave is obtained by substituting Equations C4 and C5 into C3 to compute the cross correlation between  $w'$  and  $T'$

$$\overline{w'(t)T'(t)} = -\frac{(\gamma-1)}{2\gamma H} \frac{g}{N^2} \frac{A_T^2}{\bar{T}} \frac{\frac{\omega}{m} \left( 1 - \frac{\omega^2}{N^2} \right)}{\left[ 1 + \frac{1}{(mH)^2} \left( \frac{1}{2} - \frac{\gamma-1}{\gamma} \frac{\omega^2}{N^2} \right)^2 \right]} \simeq -\frac{1}{2} \frac{g^2 A_T^2}{C_p N^2 (\bar{T})^2} \frac{\omega}{m} \simeq -\frac{A_T^2}{2\bar{T}} \frac{\omega}{m}, \quad (C6)$$

where the right-hand-side was approximated by assuming  $\omega^2 \ll N^2$ ,  $\partial T/\partial z \ll \Gamma_{ad} = g/C_p$ , and  $1 \ll 2(mH)^2$ . Gravity waves with fast vertical phase speeds and relatively large temperature amplitudes or with relatively slow vertical phase speeds but very large temperature amplitudes, can induce large positive sensible heat fluxes. These waves are relatively common in the lower thermosphere at McMurdo (e.g., Chen et al., 2016; Chu, Yu, et al., 2011), and their predicted phase shift between  $w'$  and  $T'$  to values 6–10° less than 90° can lead to large, positive sensible heat fluxes induced by upward-propagating, non-dissipating waves, as we observed.

The energy flux for an idealized individual wave can also be derived using the polarization relation given by Equation B7 in Vadas (2013),

$$\frac{p'}{\bar{\rho}} = \frac{ig}{m} \frac{\left( 1 - \frac{\omega^2}{N^2} \right)}{\left[ 1 + \frac{i}{mH} \left( \frac{1}{2} - \frac{\gamma-1}{\gamma} \frac{\omega^2}{N^2} \right) \right]} \frac{T'}{\bar{T}} = \frac{g}{m} \left( 1 - \frac{\omega^2}{N^2} \right) \frac{\exp[-i(\phi_p - \phi_T)]}{\left[ 1 + \frac{1}{(mH)^2} \left( \frac{1}{2} - \frac{\gamma-1}{\gamma} \frac{\omega^2}{N^2} \right)^2 \right]^{1/2}} \frac{T'}{\bar{T}}, \quad (C7)$$

where  $p'$  is the pressure fluctuation induced by the wave,  $\bar{\rho}$  is the mean background density, and

$$\phi_p - \phi_T = -\frac{\pi}{2} + \tan^{-1} \left[ \frac{1}{mH} \left( \frac{1}{2} - \frac{\gamma-1}{\gamma} \frac{\omega^2}{N^2} \right) \right]. \quad (C8)$$

By computing the cross correlation between  $w'$  and  $p'$  we obtain

$$\overline{w'(t)p'(t)} = \frac{1}{2} A_w A_p \cos(\phi_w - \phi_p) = -\frac{\bar{\rho} g^2}{2N^2} \frac{A_T^2}{\bar{T}^2} \frac{\frac{\omega}{m} \left( 1 - \frac{\omega^2}{N^2} \right)}{\left[ 1 + \frac{1}{(mH)^2} \left( \frac{1}{2} - \frac{\gamma-1}{\gamma} \frac{\omega^2}{N^2} \right)^2 \right]} \quad (C9)$$

where  $A_p$  is the amplitude of the pressure fluctuation, and

$$\phi_w - \phi_p = \pi + \tan^{-1} \left[ \frac{(\gamma-2)}{2\gamma mH} \right]. \quad (C10)$$

Like the heat flux, the energy flux is upward (positive) for upward propagating waves for which  $m$  is negative.

Lu, Chu, Li, et al. (2017) measured the phase difference between  $w'$  and  $T'$  for 184 mesoscale waves observed between 85 and 100 km at Table Mt., CO. They found that the mean phase difference  $\phi_w - \phi_T = 84.2^\circ$  was 2.6° larger than the phase difference of 81.6° predicted by Equation C5, which they conjectured was likely caused by dissipation associated with damping by eddy and molecular viscosity. Therefore, to compute the potential temperature  $\theta$  flux, we add additional phase small shifts  $\Delta\phi_{w'T'}$  and  $\Delta\phi_{w'p'}$  to the phase differences between  $w'$  and  $T'$  and between  $w'$  and  $p'$  to account for dissipation. In this case the exact potential temperature flux is



$$\frac{\overline{w'\theta'}}{\bar{\theta}} = \frac{\overline{w'T'}}{\bar{T}} - \kappa \frac{\overline{w'p'}}{\bar{p}} = -\frac{\kappa}{2H} \frac{g}{N^2} \frac{A_T^2}{\bar{T}^2} \frac{\omega}{\left(1 - \frac{\omega^2}{N^2}\right)} \frac{[\cos(\Delta\phi_{w'T'}) - \cos(\Delta\phi_{w'p'})]}{\left[1 + \frac{1}{(mH)^2} \left(\frac{1}{2} - \frac{(\gamma-1)}{\gamma} \frac{\omega^2}{N^2}\right)^2\right]} - \frac{g\omega}{2N^2} \frac{A_T^2}{\bar{T}^2} \frac{\left\{ \left[1 - \frac{1}{(mH)^2} \left(\frac{1}{2} - \frac{1}{\gamma}\right) \left(\frac{1}{2} - \frac{(\gamma-1)}{\gamma} \frac{\omega^2}{N^2}\right)\right] \sin(\Delta\phi_{w'T'}) - 2 \left(1 - \frac{\omega^2}{N^2}\right) \frac{(\gamma-1)(2-\gamma)}{(2\gamma mH)^2} \sin(\Delta\phi_{w'p'}) \right\}}{\left[1 + \frac{1}{(mH)^2} \left(\frac{1}{2} - \frac{(\gamma-1)}{\gamma} \frac{\omega^2}{N^2}\right)^2\right]}. \quad (C11)$$

In deriving Equation C11 we note that  $\bar{p} = \bar{\rho}R\bar{T}$ ,  $H = R\bar{T}/g$ ,  $R = C_p - C_v$ , and  $\kappa = \frac{(\gamma-1)}{\gamma} = R/C_p$ . It is easier to interpret  $\overline{w'\theta'}$  if we simplify Equation C11 by noting that for weak dissipation  $\Delta\phi_{w'T'}$  and  $\Delta\phi_{w'p'}$  are only a few degrees (Lu, Chu, Li, et al., 2017) and we consider the case where  $1 \ll (mH)^2$ . Under these conditions the potential temperature flux reduces to

$$\overline{w'\theta'} \simeq -\frac{g\omega\bar{\theta}}{2N^2} \frac{A_T^2}{\bar{T}^2} \sin(\Delta\phi_{w'T'}). \quad (C12)$$

The small phase shifts between  $w'$  and  $p'$  caused by dissipation and compressibility are negligible because these fluctuations are nearly  $180^\circ$  out of phase. In contrast, the small phase shifts between  $w'$  and  $T'$  are significant because these fluctuations are approximately  $90^\circ$  out of phase. If there is no dissipation  $\Delta\phi_{w'T'} = 0$  and  $\Delta\phi_{w'p'} = 0$ , the contributions to  $\overline{w'\theta'}$  from the heat and energy fluxes cancel each other and according to Equations C11 and C12,  $\overline{w'\theta'} = 0$ .

## Data Availability Statement

The data shown in this work can be downloaded in MatLab data format from Mendeley Data repository <https://data.mendeley.com/datasets/6t76ty4rjj/2>. Aurora image data are available online from NIPR website (<http://pc115.seg20.nipr.ac.jp/www/AQVN/index.html>).

## Acknowledgments

We sincerely appreciate Dr. Sharon Vadas and Dr. Erich Becker for their advice and invaluable discussion on the compressible polarization relations for gravity waves and on energetics and wave dynamics of the middle and upper atmosphere. We are grateful to Jackson Jandreau for his assistance in compiling satellite and WACCM data of minor species for chemical flux calculation, to Wuhu Feng for providing WACCM  $K_{zz}$  data, to Tao Li for providing the Hefei flux measurements, and to Juan Diego Carrillo-Sanchez for providing CABMOD meteoric injection rates. We gratefully acknowledge Dr. Art Richmond, Dr. Yasunobu Ogawa, Dr. Zhonghua Xu, and Dr. Yukitoshi Nishimura for invaluable discussions on heat sources and heat balance in the lower thermosphere. We are grateful to Dr. Yasunobu Ogawa for providing aurora observations at McMurdo. We sincerely appreciate the staff of United States Antarctic Program, McMurdo Station, Antarctica New Zealand, and Scott Base for their superb support to the McMurdo lidar observations. The McMurdo lidar projects were supported by the National Science Foundation (NSF) grants OPP-1246405, OPP-1443726, and OPP-2110428. This work was partially supported by NSF grants AGS-2029162 and AGS-1452351. The auroral images were obtained with supports from NSF (ANT-1643700) and the Japanese Antarctic Research Expedition program (AP0927).

## References

- Allen, S. J., & Vincent, R. A. (1995). Gravity wave activity in the lower atmosphere: Seasonal and latitudinal variations. *Journal of Geophysical Research*, 100(D1), 1327–1350. <https://doi.org/10.1029/94jd02688>
- Beagley, S. R., Boone, C. D., Fomichev, V. I., Jin, J. J., Semeniuk, K., McConnell, J. C., & Bernath, P. F. (2010). First multi-year occultation observations of  $\text{CO}_2$  in the MLT by ACE satellite: Observations and analysis using the extended CMAM. *Atmospheric Chemistry and Physics*, 10(3), 1133–1153. <https://doi.org/10.5194/acp-10-1133-2010>
- Becker, E., & Vadas, S. L. (2018). Secondary gravity waves in the winter mesosphere: Results from a high-resolution global circulation model. *Journal of Geophysical Research: Atmospheres*, 123(5), 2605–2627. <https://doi.org/10.1002/2017JD027460>
- Carrillo-Sánchez, J. D., Gomez-Martin, J. G., Bones, D. L., Nesvorný, D., Pokorný, P., Benna, M., et al. (2020). Cosmic dust fluxes in the atmospheres of Earth, Mars, and Venus. *Icarus*, 335(1), 113395. <https://doi.org/10.1016/j.icarus.2019.113395>
- Carrillo-Sánchez, J. D., Nesvorný, D., Pokorný, P., Janches, D., & Plane, J. M. C. (2016). Sources of cosmic dust in the Earth's atmosphere. *Geophysical Research Letters*, 43(23), 11979–11986. <https://doi.org/10.1002/2016GL071697>
- Carrillo-Sánchez, J. D., Plane, J. M. C., Feng, W., Nesvorný, D., & Janches, D. (2015). On the size and velocity distribution of cosmic dust particles entering the atmosphere. *Geophysical Research Letters*, 42(15), 6518–6525. <https://doi.org/10.1002/2015GL065149>
- Chen, C., & Chu, X. (2017). Two-dimensional Morlet wavelet transform and its application to wave recognition methodology of automatically extracting two-dimensional wave packets from lidar observations in Antarctica. *Journal of Atmospheric and Solar-Terrestrial Physics*, 162, 28–47. <https://doi.org/10.1016/j.jastp.2016.10.016>
- Chen, C., Chu, X., McDonald, A. J., Vadas, S. L., Yu, Z., Fong, W., & Lu, X. (2013). Inertia-gravity waves in Antarctica: A case study using simultaneous lidar and radar measurements at McMurdo/Scott Base (77.8°S, 166.7°E). *Journal of Geophysical Research: Atmospheres*, 118(7), 2794–2808. <https://doi.org/10.1002/jgrd.50318>
- Chen, C., Chu, X., Zhao, J., Roberts, B. R., Yu, Z., Fong, W., et al. (2016). Lidar observations of persistent gravity waves with periods of 3–10 h in the Antarctic middle and upper atmosphere at McMurdo (77.83°S, 166.67°E). *Journal of Geophysical Research: Space Physics*, 121(2), 1483–1502. <https://doi.org/10.1002/2015ja022127>
- Chu, X., Gardner, C. S., & Franke, S. J. (2005). Nocturnal thermal structure of the mesosphere and lower thermosphere region at Maui, Hawaii (20.7°N), and Starfire Optical Range, New Mexico (35°N). *Journal of Geophysical Research*, 110(D9), D09S03. <https://doi.org/10.1029/2004JD004891>
- Chu, X., Gardner, C. S., Li, X., & Lin, Y.-T. (2022). Vertical transport of sensible heat and meteoric Na by the complete temporal spectrum of gravity waves in the MLT above McMurdo (77.84°S, 166.67°E), Antarctica (version 2). [Dataset]. Mendeley Data. <https://doi.org/10.17632/6t76ty4rjj.2>
- Chu, X., Huang, W., Fong, W., Yu, Z., Wang, Z., Smith, J. A., & Gardner, C. S. (2011). First lidar observations of polar mesospheric clouds and Fe temperatures at McMurdo (77.8°S, 166.7°E), Antarctica. *Geophysical Research Letters*, 38(16), L16810. <https://doi.org/10.1029/2011GL048373>
- Chu, X., Nishimura, Y., Xu, Z., Yu, Z., Plane, J. M. C., Gardner, C. S., & Ogawa, Y. (2020). First simultaneous lidar observations of thermosphere-ionosphere Fe and Na (TlFe and TlNa) layers at McMurdo (77.84°S, 166.67°E), Antarctica with concurrent measurements of

- aurora activity, enhanced ionization layers, and converging electric field. *Geophysical Research Letters*, 47(20), e2020GL090181. <https://doi.org/10.1029/2020GL090181>
- Chu, X., & Papen, G. (2005). Resonance fluorescence lidar for measurements of the middle and upper atmosphere. In T. Fujii & T. Fukuchi (Eds.), *Laser remote sensing* (pp. 179–432). CRC Press. <https://doi.org/10.1201/9781420030754>
- Chu, X., Yu, Z., Gardner, C. S., Chen, C., & Fong, W. (2011). Lidar observations of neutral Fe layers and fast gravity waves in the thermosphere (110–155 km) at McMurdo (77.8°S, 166.7°E), Antarctica. *Geophysical Research Letters*, 38(23). <https://doi.org/10.1029/2011GL050016>
- Chu, X., Zhao, J., Lu, X., Harvey, V. L., Jones, R. M., Becker, E., et al. (2018). Lidar observations of stratospheric gravity waves from 2011 to 2015 at McMurdo (77.84°S, 166.69°E), Antarctica: 2. Potential energy densities, lognormal distributions, and seasonal variations. *Journal of Geophysical Research: Atmospheres*, 123(15), 7910–7934. <https://doi.org/10.1029/2017JD027386>
- Coy, L., Fritts, D. C., & Weinstock, J. (1986). The Stokes drift due to vertically propagating internal gravity waves in a compressible atmosphere. *Journal of the Atmospheric Sciences*, 43(22), 2636–2643. [https://doi.org/10.1175/1520-0469\(1986\)043<2636:TSDDTV>2.0.CO;2](https://doi.org/10.1175/1520-0469(1986)043<2636:TSDDTV>2.0.CO;2)
- Dimant, Y. S., & Oppenheim, M. M. (2011a). Magnetosphere-ionosphere coupling through E region turbulence: 1. Energy budget. *Journal of Geophysical Research*, 116(A9), A09303. <https://doi.org/10.1029/2011JA016648>
- Dimant, Y. S., & Oppenheim, M. M. (2011b). Magnetosphere-ionosphere coupling through E region turbulence: 2. Anomalous conductivities and frictional heating. *Journal of Geophysical Research*, 116(A9), A09304. <https://doi.org/10.1029/2011JA016649>
- Fong, W., Chu, X., Lu, X., Chen, C., Fuller-Rowell, T. J., Codrescu, M., & Richmond, A. D. (2015). Lidar and CTIPe model studies of the fast amplitude growth with altitude of the diurnal temperature “tides” in the Antarctic winter lower thermosphere and dependence on geomagnetic activity. *Geophysical Research Letters*, 42(3), 697–704. <https://doi.org/10.1002/2014GL062784>
- Fong, W., Lu, X., Chu, X., Fuller-Rowell, T. J., Yu, Z., Roberts, B. R., et al. (2014). Winter temperature tides from 30 to 110 km at McMurdo (77.8°S, 166.7°E), Antarctica: Lidar observations and comparisons with WAM. *Journal of Geophysical Research: Atmospheres*, 119(6), 2846–2863. <https://doi.org/10.1002/2013JD020784>
- Gardner, C. S. (2018). Role of wave-induced diffusion and energy flux in the vertical transport of atmospheric constituents in the mesopause region. *Journal of Geophysical Research: Atmospheres*, 123(12), 6581–6604. <https://doi.org/10.1029/2018JD028359>
- Gardner, C. S., & Chu, X. (2020). Eliminating photon noise biases in the computation of second-order statistics of lidar temperature, wind, and species measurements. *Applied Optics*, 59(27), 8259–8271. <https://doi.org/10.1364/AO.400375>
- Gardner, C. S., Guo, Y., & Liu, A. Z. (2019). Parameterizing wave-driven vertical constituent transport in the upper atmosphere. *Earth and Space Science*, 6, 904–913. <https://doi.org/10.1029/2019EA000625>
- Gardner, C. S., & Liu, A. Z. (2007). Seasonal variations of the vertical fluxes of heat and horizontal momentum in the mesopause region at Starfire Optical Range, New Mexico. *Journal of Geophysical Research*, 112(D9), D09113. <https://doi.org/10.1029/2005JD006179>
- Gardner, C. S., & Liu, A. Z. (2010). Wave-induced transport of atmospheric constituents and its effect on the mesospheric Na layer. *Journal of Geophysical Research*, 115(D20), D20302. <https://doi.org/10.1029/2010JD014140>
- Gardner, C. S., & Liu, A. Z. (2016). Chemical transport of neutral atmospheric constituents by waves and turbulence: Theory and observations. *Journal of Geophysical Research: Atmospheres*, 121(1), 494–520. <https://doi.org/10.1002/2015JD023145>
- Gardner, C. S., Liu, A. Z., & Guo, Y. (2016). Vertical and horizontal transport of mesospheric Na: Implications for the mass influx of cosmic dust. *Journal of Atmospheric and Solar-Terrestrial Physics*, 162, 192–202. <https://doi.org/10.1016/j.jastp.2016.07.013>
- Gardner, C. S., & Yang, W. (1998). Measurements of the dynamical cooling rate associated with the vertical transport of heat by dissipating gravity waves in the mesopause region at the Starfire Optical Range, New Mexico. *Journal of Geophysical Research*, 103(D14), 16909–16926. <https://doi.org/10.1029/98JD00683>
- Gavrilov, N. M., Fukao, S., Nakamura, T., Tsuda, T., Yamanaka, M. D., & Yamamoto, M. (1996). Statistical analysis of gravity waves observed with the middle and upper atmosphere radar in the middle atmosphere: 1. Method and general characteristics. *Journal of Geophysical Research*, 101(D23), 29511–29521. <https://doi.org/10.1029/96JD01447>
- Grygashvily, M., Becker, E., & Sonnemann, G. R. (2012). Gravity wave mixing and effective diffusivity for minor chemical constituents in the mesosphere/lower thermosphere. *Space Science Reviews*, 168(1–4), 333–362. <https://doi.org/10.1007/s11214-011-9857-x>
- Guo, Y., & Liu, A. Z. (2021). Seasonal variation of vertical heat and energy fluxes due to dissipating gravity waves in the mesopause region over the Andes. *Journal of Geophysical Research: Atmospheres*, 126(3), e2020JD033825. <https://doi.org/10.1029/2020JD033825>
- Hickey, M. P., Walterscheid, R. L., & Richards, P. G. (2000). Secular variations of atomic oxygen in the mesopause region induced by transient gravity wave packets. *Geophysical Research Letters*, 27(21), 3599–3602. <https://doi.org/10.1029/2000GL011953>
- Holton, J. R. (1982). The role of gravity wave induced drag and diffusion in the momentum budget of the mesosphere. *Journal of the Atmospheric Sciences*, 39(4), 791–799. [https://doi.org/10.1175/1520-0469\(1982\)039<0791:TROGWI>2.0.CO;2](https://doi.org/10.1175/1520-0469(1982)039<0791:TROGWI>2.0.CO;2)
- Holton, J. R. (1983). The influence of gravity wave breaking on the circulation of the middle atmosphere. *Journal of the Atmospheric Sciences*, 40(10), 2497–2507. [https://doi.org/10.1175/1520-0469\(1983\)040<2497:TIOGWB>2.0.CO;2](https://doi.org/10.1175/1520-0469(1983)040<2497:TIOGWB>2.0.CO;2)
- Hu, X., Liu, A. Z., Gardner, C. S., & Swenson, G. R. (2002). Characteristics of quasi-monochromatic gravity waves observed with Na lidar in the mesopause region at Starfire Optical Range, NM. *Geophysical Research Letters*, 29(24), 2169–224. <https://doi.org/10.1029/2002GL014975>
- Huang, W., Chu, X., Gardner, C. S., Carrillo-Sánchez, J. D., Feng, W., Plane, J. M. C., & Nesvorný, D. (2015). Measurements of the vertical fluxes of atomic Fe and Na at the mesopause: Implications for the velocity of cosmic dust entering the atmosphere. *Geophysical Research Letters*, 42(1), 169–175. <https://doi.org/10.1002/2014GL062390>
- Kurihara, J., Oyama, S., Nozawa, S., Tsuda, T. T., Fujii, R., Ogawa, Y., et al. (2009). Temperature enhancements and vertical winds in the lower thermosphere associated with auroral heating during the DELTA campaign. *Journal of Geophysical Research*, 114(A12), A12306. <https://doi.org/10.1029/2009JA014392>
- Lindzen, R. S. (1981). Turbulence and stress owing to gravity wave and tidal breakdown. *Journal of Geophysical Research*, 86(C10), 9707–9714. <https://doi.org/10.1029/JC086iC10p09707>
- Liu, A. Z. (2009). Estimate eddy diffusion coefficients from gravity wave vertical momentum and heat fluxes. *Geophysical Research Letters*, 36(8), L08806. <https://doi.org/10.1029/2009GL037495>
- Liu, A. Z., & Gardner, C. S. (2004). Vertical dynamical transport of mesospheric constituents by dissipating gravity waves. *Journal of Atmospheric and Solar-Terrestrial Physics*, 66(3–4), 267–275. <https://doi.org/10.1016/j.jastp.2003.11.002>
- Liu, A. Z., & Gardner, C. S. (2005). Vertical heat and constituent transport in the mesopause region by dissipating gravity waves at Maui, Hawaii (20.7°N), and Starfire Optical Range, New Mexico (35°N). *Journal of Geophysical Research*, 110(D9), D09S13. <https://doi.org/10.1029/2004JD004965>
- Liu, A. Z., & Guo, Y. (2016). Photomultiplier tube calibration based on Na lidar observation and its effect on heat flux bias. *Applied Optics*, 55(33), 9467–9475. <https://doi.org/10.1364/AO.55.009467>
- Liu, H.-L. (2021). Effective vertical diffusion by atmospheric gravity waves. *Geophysical Research Letters*, 48(1), e2020GL091474. <https://doi.org/10.1029/2020GL091474>

- Lu, X., Chu, X., Chen, C., Nguyen, V., & Smith, A. K. (2017). First observations of short-period eastward propagating planetary waves from the stratosphere to the lower thermosphere (110 km) in winter Antarctica. *Geophysical Research Letters*, 44(20), 10744–10753. <https://doi.org/10.1002/2017GL075641>
- Lu, X., Chu, X., Fuller-Rowell, T., Chang, L., Fong, W., & Yu, Z. (2013). Eastward propagating planetary waves with periods of 1–5 days in the winter Antarctic stratosphere as revealed by MERRA and lidar. *Journal of Geophysical Research: Atmospheres*, 118(17), 9565–9578. <https://doi.org/10.1002/jgrd.50717>
- Lu, X., Chu, X., Li, H., Chen, C., Smith, J. A., & Vadas, S. L. (2017). Statistical characterization of high-to-medium frequency mesoscale gravity waves by lidar-measured vertical winds and temperatures in the MLT. *Journal of Atmospheric and Solar-Terrestrial Physics*, 162, 3–15. <https://doi.org/10.1016/j.jastp.2016.10.009>
- Mlynarczyk, M. G., & Solomon, S. (1993). A detailed evaluation of the heating efficiency in the middle atmosphere. *Journal of Geophysical Research*, 98(D6), 10517–10541. <https://doi.org/10.1029/93JD00315>
- Ogawa, Y., Tanaka, Y., Kadokura, A., Hosokawa, K., Ebihara, Y., Motoba, T., et al. (2020). Development of low-cost multi-wavelength imager system for studies of aurora and airglow. [Dataset]. *Polar Science*, 23, 100501. <https://doi.org/10.1016/j.polar.2019.100501>
- Pfenninger, M., Liu, A. Z., Papen, G. C., & Gardner, C. S. (1999). Gravity wave characteristics in the lower atmosphere at South Pole. *Journal of Geophysical Research*, 104(D6), 5963–5984. <https://doi.org/10.1029/98JD02705>
- Picone, J. M., Hedin, A. E., Drob, D. P., & Aikin, A. C. (2002). NRLMSISE-00 empirical model of the atmosphere: Statistical comparisons and scientific issues. *Journal of Geophysical Research*, 107(A12), SIA 15–1–SIA 15–16. <https://doi.org/10.1029/2002JA009430>
- Plane, J. M. C., Feng, W., & Dawkins, E. C. M. (2015). The mesosphere and metals: Chemistry and changes. *Chemical Reviews. Special Issue: 2015 Chemistry in Climate*, 115(10), 4497–4541. <https://doi.org/10.1021/cr500501m>
- She, C. Y., & Yu, J. R. (1994). Simultaneous three-frequency Na lidar measurements of radial wind and temperature in the mesopause region. *Geophysical Research Letters*, 21(17), 1771–1774. <https://doi.org/10.1029/94GL01417>
- Sinnhuber, M., Nieder, H., & Wieters, N. (2012). Energetic particle precipitation and the chemistry of the mesosphere/lower thermosphere. *Surveys in Geophysics*, 33(6), 1281–1334. <https://doi.org/10.1007/s10712-012-9201-3>
- Smith, J. A., & Chu, X. (2015). High-efficiency receiver architecture for resonance-fluorescence and Doppler lidars. *Applied Optics*, 54(11), 3173–3184. <https://doi.org/10.1364/AO.54.003173>
- Strelnikova, I., Baumgarten, G., & Lübken, F.-J. (2020). Advanced hodograph-based analysis technique to derive gravity-wave parameters from lidar observations. *Atmospheric Measurement Techniques*, 13(2), 479–499. <https://doi.org/10.5194/amt-13-479-2020>
- Tao, X., & Gardner, C. S. (1995). Heat flux observations in the mesopause region above Haleakala. *Geophysical Research Letters*, 22(20), 2829–2832. <https://doi.org/10.1029/95GL02876>
- Thayer, J. P., & Semeter, J. (2004). The convergence of magnetospheric energy flux in the polar atmosphere. *Journal of Atmospheric and Solar-Terrestrial Physics*, 66(10), 807–824. <https://doi.org/10.1016/j.jastp.2004.01.035>
- Vadas, S. L. (2013). Compressible f-plane solutions to body forces, heatings, and coolings, and application to the primary and secondary gravity waves generated by a deep convective plume. *Journal of Geophysical Research: Space Physics*, 118(5), 2377–2397. <https://doi.org/10.1002/jgra.50163>
- Vadas, S. L., & Becker, E. (2018). Numerical modeling of the excitation, propagation, and dissipation of primary and secondary gravity waves during wintertime at McMurdo Station in the Antarctic. *Journal of Geophysical Research: Atmospheres*, 123(17), 9326–9369. <https://doi.org/10.1029/2017JD027974>
- Vadas, S. L., & Becker, E. (2019). Numerical modeling of the generation of tertiary gravity waves in the mesosphere and thermosphere during strong mountain wave events over the Southern Andes. *Journal of Geophysical Research: Space Physics*, 124(9), 7687–7718. <https://doi.org/10.1029/2019JA026694>
- Vadas, S. L., Fritts, D. C., & Alexander, M. J. (2003). Mechanism for the generation of secondary waves in wave breaking regions. *Journal of the Atmospheric Sciences*, 60(1), 194–214. [https://doi.org/10.1175/1520-0469\(2003\)060<0194:Mftgos>2.0.CO;2](https://doi.org/10.1175/1520-0469(2003)060<0194:Mftgos>2.0.CO;2)
- Vadas, S. L., Zhao, J., Chu, X., & Becker, E. (2018). The excitation of secondary gravity waves from local body forces: Theory and observation. *Journal of Geophysical Research: Atmospheres*, 123(17), 9296–9325. <https://doi.org/10.1029/2017JD027970>
- Walterscheid, R. L. (1981). Dynamical cooling induced by dissipating internal gravity waves. *Geophysical Research Letters*, 8(12), 1235–1238. <https://doi.org/10.1029/GL008i012p01235>
- Walterscheid, R. L., & Hickey, M. P. (2009). Gravity wave ducting in the upper mesosphere and lower thermosphere duct system. *Journal of Geophysical Research*, 114(D19), D19109. <https://doi.org/10.1029/2008JD011269>
- Walterscheid, R. L., & Hocking, W. K. (1991). Stokes diffusion by atmospheric internal gravity waves. *Journal of the Atmospheric Sciences*, 48(20), 2213–2230. [https://doi.org/10.1175/1520-0469\(1991\)048<2213:SDBAIG>2.0.CO;2](https://doi.org/10.1175/1520-0469(1991)048<2213:SDBAIG>2.0.CO;2)
- Walterscheid, R. L., & Schubert, G. (1989). Gravity wave fluxes of O<sub>3</sub> and OH at the night-side mesopause. *Geophysical Research Letters*, 16(7), 719–722. <https://doi.org/10.1029/GL016i007p00719>
- Wang, L., Geller, M. A., & Alexander, M. J. (2005). Spatial and temporal variations of gravity wave parameters, Part I: Intrinsic frequency, wavelength, and vertical propagation direction. *Journal of the Atmospheric Sciences*, 62(1), 125–142. <https://doi.org/10.1175/JAS-3364.1>
- Weinstock, J. (1983). Heat flux induced by gravity waves. *Geophysical Research Letters*, 10(2), 165–167. <https://doi.org/10.1029/GL010i002p00165>
- Yu, Y., & Hickey, M. P. (2007). Numerical modeling of a gravity wave packet ducted by the thermal structure of the atmosphere. *Journal of Geophysical Research*, 112(A6), A06308. <https://doi.org/10.1029/2006JA012092>
- Zhao, J., Chu, X., Chen, C., Lu, X., Fong, W., Yu, Z., et al. (2017). Lidar observations of stratospheric gravity waves from 2011 to 2015 at McMurdo (77.84°S, 166.69°E), Antarctica: I. Vertical wavelengths, periods, and frequency and vertical wave number spectra. *Journal of Geophysical Research: Atmospheres*, 122(10), 5041–5062. <https://doi.org/10.1002/2016JD026368>